JOHNS HOPKINS
APPLIED PHYSICS LABORATORY

Analysis of Alternatives for Near Earth Object Detection, Tracking and Characterization

Final Report

November 08, 2018

Analysis of Alternatives for Near Earth Object Detection, Tracking and Characterization Report

1. Introduction and Background

The goal of the Planetary Defense Initiative Analysis of Alternatives (AoA) study was to trade the cost and performance of a Near Earth Object (NEO) survey system to track, detect and characterize ≥90% of NEOs of ≥140 m diameter over 10-year lifetime. The questions the study was tasked to answer were:

- What system or a mix of systems provides the nation the best balance between effectiveness and affordability addressing NEO survey gaps?
- What balance of space-based sensors would best augment the existing and planned ground-based capabilities and provide the overall best solution for the survey challenges.

The study assumed baseline Program of Record (POR) and run it out to 2033. The NEO synthetic population was modeled on the Science Definition Team (SDT) 2017 report. An NEO was to be counted as tracked and its orbit determined if it was detected with Signal to Noise (SNR) of 5 or greater, and 3 tracklets were acquired over 25 days where tracklet was defined as 3 detections, requiring at least 4 image frames within ~24 hours. The alternatives had to achieve the survey goal within ~10 years, and cost less $400M Phases A-D (FY17), excluding Launch Vehicle. The technology needed to be at ≥ TRL 6 by mission PDR.

The study was conducted between late May and October of 2017. The flow for study is shown in ***Figure 1***. A variety of cases were investigated that included assets in LEO, GEO and L1 orbits, as well as Earth Moon resonance orbits. The conclusion at that time was that separating detection, which could be done using VIS (visible) telescopes, and characterization, which could be done using infrared (IR) telescopes, would allow for a more phased approach in a cost-constrained climate. In October 2017, the study was briefed out to NASA sponsors. More follow-on work was conducted to understand whether a solution existed for the International Space Station (ISS), whether the study's rate of asteroid detections was correct, and whether the Mission Operations and Ground costs (MODC) were adequately accounted for. An error in zodiacal background was identified, and the model was more rigorously evaluated by comparing the SDT (MIT Lincoln Laboratory) and NASA Goddard Space Flight Center (GSFC) models for visible telescopes. The model continues to be in disagreement with the SDT assessment for infrared telescopes. The detailed alternatives proposed in October 2017 were remodeled with the new backgrounds and were found not to meet the goals as defined in the study. Additional work was performed in May – September 2018 to compare the AoA and SDT IR models, resulting in better agreement.

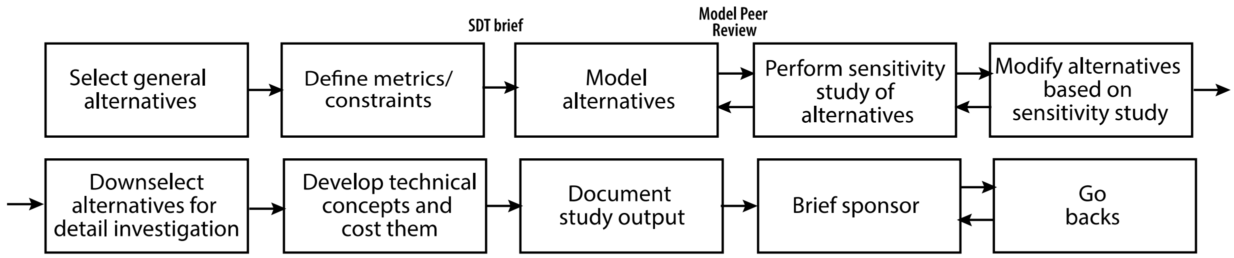

__Figure 1__ Analysis of Alternatives process. The strategy was to validate models with SDT 2017 results, but don't repeat what SDT has done or what previously was investigated by SDTs or other teams previously (e.g. remove Venus and L2 orbits as expensive alternatives). A detailed assessment of the payload and spacecraft (s/c) bus subsystems were performed to increase fidelity of system, architecture and costs. There was an explicit focus on "operations" type mode, with science not being the primary focus of the study. The promising alternatives were costed consistent with SDT for apples-to-apples comparisons. All payload and s/c bus systems were parametrically modeled using detail on mass, power, data rate, etc. In addition, several resources were leveraged to increase confidence of cost estimates and to assess risk.

Section 2 of the report covers the overall architecture of the NEO simulation model, the NEO and Potentially Hazardous Objects (PHO) population modeling, cadences and revisit strategy, backgrounds and sensor modeling. The results of the simulations and the validation with SDT and GSFC are also shown. **Sections 3** and **4** describe the payload and spacecraft bus that were used for the downselected alternatives. **Section 5** describes the trajectory design for the alternatives. Cost estimation is described in **Section 6**, with discussion, conclusions and recommendations in **Section 7**. References are provided at the end of the report.

2. Model

2.1 Overall architecture

The JHU/APL NEO survey modeling and simulation tool was developed to assess the effectiveness of NEO observation systems, for both ground- and space-based platforms. One particular goal is to assess the improvements a space-based survey system would offer when used in addition to a baseline ground architecture. The fundamental question addressed is: Given an asteroid population and one or more sensors (ground and/or space, IR and/or visible), how well does the system perform in detecting NEOs (or a subset) over a given time period?

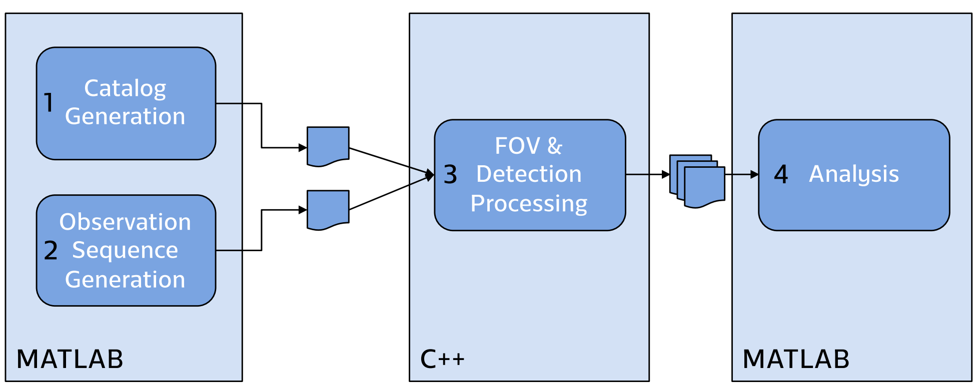

__Figure 2__ The overall architecture of the JHU/APL NEO survey simulation

The simulation is broken down into three main stages as shown in the ***Figure 2***. Each stage outputs one or more files that can be independently assessed and validated before being passed to the next stage.

The first stage involves the generation of a synthetic asteroid population and observation cadence. The step is run offline multiple times to generate a variety of catalogs and observation sequences. Catalogs are generated randomly from a set of distributions, thus allowing for statistical analyses, and can be generated for all near-Earth objects or just potentially hazardous objects. In general, the simulation uses synthetic catalogs that are much larger than the estimated real NEO and PHA populations for statistical analysis to estimate potential real-world sensor system performance. The observation sequence drives the time steps taken in the next stage of the simulation.

The second stage is the core simulation processing, which handles simulated asteroid imaging and detection processing and outputs asteroids in the FOV at each time step and whether or not those asteroids were detected. The catalog generated in stage one is used to generate the position of the asteroids relative to the sensor field of view.

The final stage is analysis, which with cataloging completeness and other metrics are computed.

2.2 Core Simulation Processing – Imaging, FOV, and Detections

The core simulation processing works as follows. For each time step t (from cadence):

1. Propagate all asteroids forward to time t, using Keplerian propagation (for speed)
2. Determine which objects are in FOV
3. Of objects in FOV, determine which can be "detected" (discussion to follow)

After that process is completed for all time steps, the resultant output contains, for every time step, a list of objects in the FOV, those object's computed SNR, and other ancillary metadata. The output is passed to the analysis tools to determine which objects are considered detectable for cataloging.

To determine whether a detected object can be cataloged, the number and timing of its detections are analyzed. An object is considered cataloged if a valid "track" of three valid "tracklets", each containing three detections, can be assembled. A tracklet is valid if its first and last detection are no more than twenty-four hours apart, and a track is considered valid if its tracklets are separated by at least twenty-four hours and its first and last tracklets are no more than twenty-five days apart. These timing requirements are based on the needs of linking and orbit determination algorithms, but the simulation does not explicitly perform linking or orbit determination.

2.3 Sensor Model

For the purposes of a field-of-view model, the sensors in the simulation are considered to be pinhole cameras, as illustrated in ***Figure 3:***

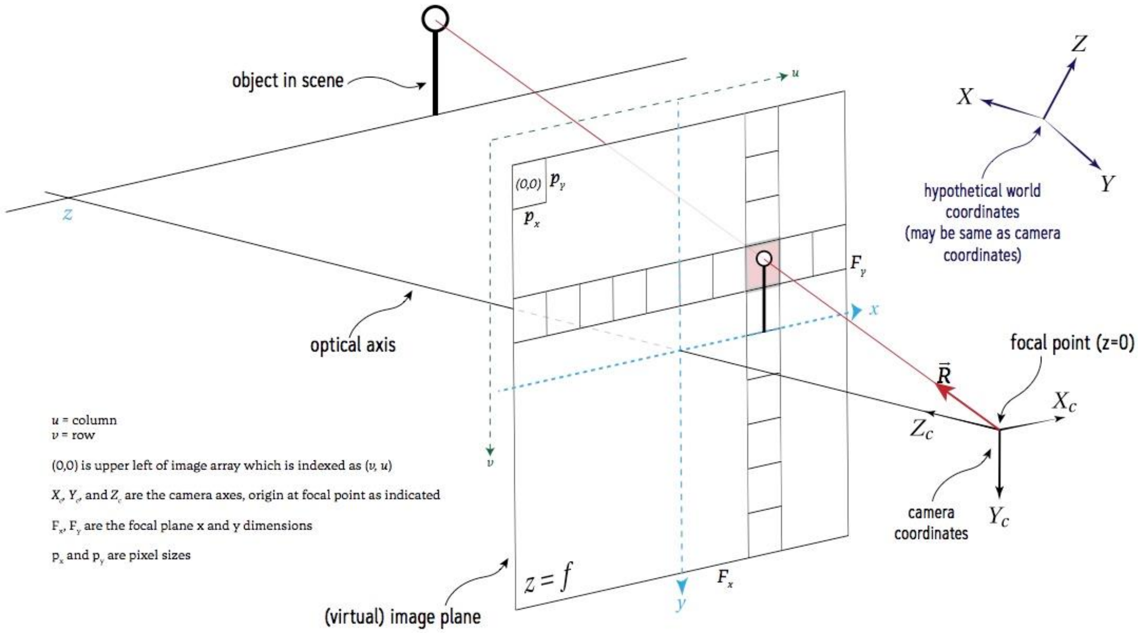

Figure 3 *Sensor Model representation*

The optical model also includes the following properties:

- Effective aperture area, which can account for obscurations such as from a secondary mirror.
- System optical speed (f-number).
- Spectral transmission through each of the system reflective and transmissive elements).
- Optical point spread function (PSF), which is modeled as a Gaussian with some given full-width at half maximum. The PSF also accounts for any potential high-frequency jitter in the sensor system. To account for other effects, such as degradation due to atmospheric effects, modeled seeing is convolved with the estimated optical PSF.

The focal plane array model includes the following:

- Physical properties: size of the FPA and FPA elements (pixels) and an array mask that accounts for gaps between individual array elements, dead pixels, etc.
- Noise terms: dark current (as a function of detector temperature for IR systems, modeled using Rule 07) (Tennant et al., 2008) readout noise level, and additive and multiplicative residual non-uniformity (modeling the effects of errors in FPA calibration).
- Spectral quantum efficiency.
- Pixel electron well depth: determines how much signal can be collected in one pixel and sets the FPA saturation level.
- Integration time.

A particular sensor can be simulated to have multiple FPAs, with arbitrary gaps between those FPAs.

2.4 Detection Processing

Given the sensor model (***Figure 3***) and the asteroid catalog, the simulation first determines which objects are within the field of view, by computing where on the focal plane the light from each asteroid might fall, in the sensor frame of reference. Those objects that are determined to fall outside the FPA bounds are rejected. Then, of those objects that fall within the FPA bounds, some are rejected if it is determined that the signal falls on a gap in the focal plane or on a dead pixel (based on the FPA mask). Of those objects that remain, the objects' intensity and irradiance at the detector are computed (to be described in a later section), and a signal-to-noise ratio (SNR) computed.

Within this simulation it is the single pixel signal-to-noise ratio that's computed and used to determine detectability of the asteroid. Given the asteroid's irradiance, the signal electrons S_e are computed as follows:

$$S_e = \frac{1}{hc} A_{eff} \tau k_{sf} \int_{\lambda_1}^{\lambda_2} E_A(\lambda) Q_e(\lambda) T(\lambda) \lambda d\lambda$$

where A_{eff} is the effective sensor aperture area, τ the integration time, k_{sf} the straddle factor (see below), $E_A(\lambda)$ the asteroid irradiance as a function of wavelength, $Q_e(\lambda)$ the quantum efficiency as a function of wavelength, and $T(\lambda)$ the telescope transmission as a function of wavelength, all integrated over the sensor waveband specified by λ_1 and λ_2.

Then, given some background irradiance, the background signal in electrons is computed as follows (note that the IFOV is already accounted for in irradiance estimate):

$$B_e = \frac{1}{hc} A_{eff} \tau \int_{\lambda_1}^{\lambda_2} E_B(\lambda) Q_e(\lambda) T(\lambda) \lambda d\lambda$$

The noise within one pixel is the RSS of the various noise terms (assumed to the be independent):

$$N_e = \sqrt{S_e + B_e + D_e + R^2 + (\gamma_M \overline{D_e})^2 + (\gamma_A \overline{B_e})^2}$$

Where D_e is the dark current electrons during the integration time, R the RMS read noise, γ_M the non-uniformity residual expected from detector calibration to take out dark current non-uniformity, and γ_A the correction residual expected from background correction. The value of the non-uniformity term depends on detector specifics (e.g. manufacturing precision in pixel size), the calibration method used, and changes as a function of detector properties, including temperature and lifetime (e.g., radiation damage over time increases the non-uniformity). For these simulations, a value of 2% was chosen as the nominal value for detector non-uniformity residual. This value was derived from assessment of existing sensor systems developed at JHU/APL, and also reflected in other assessments considered [ORS-5, 2015; Willers et al., 2017; Hanna et al., 2016; Schulz and Caldwell, 1995]. The systems considered in [ORS-5, 2015] are visible detector systems; infrared systems generally exhibit larger non-uniformity values due to the nature of the technology [Willers et al., 2017; Hanna et al., 2016; Schulz and Caldwell, 1995]. However, APL's simulations of both visible and IR systems used the 2% value, and it is expected that space-based IR survey systems will perform frequent calibration, limiting the resulting non-uniformity residuals. To drop below the background shot noise (usually the next highest contribution), the value would need to be less than 0.1% (20x lower). Continuous flat-fielding technique allows to limit the contribution by non-uniformity residual, as shown in ***Section 2.10.3***.

The final SNR calculation first accounts for pixel saturation by limiting the maximum possible electrons S_e to the well depth, and then is computed as the ratio of the signal electrons and the noise electrons.

2.5 Straddle Factor

In general, the spot size on the FPA of an asteroid is on the same size scale as a pixel, but lights up multiple pixels due to blurring. The brightest pixel sees only some fraction of the total energy, which is often measured as the ensquared energy — the amount of energy falling within a single pixel assuming that the object is centered within that pixel. However, given that the spot can fall anywhere within a pixel, the simulation uses a statistical measure for the expected value of the fraction of light falling within the brightest pixel assuming that the spot can fall anywhere within a pixel. This term is computed as:

$$k_{SF} = \left[\mathrm{erf}\frac{\left(\frac{d}{\sqrt{2}\sigma}\right) + \sqrt{\frac{2}{\pi}}\,\sigma}{d}\left(\exp\left(-\frac{d^2}{2\sigma^2}\right) - 1\right)\right]^2$$

where sigma is the angular spread of the PSF of the system, and d is the pixel IFOV.

2.6 Modeling Asteroid Brightness

The compute asteroid brightness (radiometric intensity), the simulation uses the generated asteroid catalog to provide the asteroid's location relative to the Sun and Earth, and asteroid properties: size, visual albedo, and thermal emissivity. For asteroid brightness in the visible waveband, the primary source of light is solar reflection. In the thermal infrared (IR), we use one of three thermal models.

2.6.1. Visible

Asteroids are assumed Lambertian spheres with a given diameter *D* and albedo *ρ*, at a distance *R* from the sensor and distance *L* from the sun (in AU). Then, the asteroid's irradiance at the sensor can be computed using the equation

$$E_{sensor}(\lambda) = \frac{E_{sun,1AU}(\lambda)\pi D^2 \rho(\lambda)\Theta(\Phi)}{4L^2R^2}$$

$\Theta(\Phi)$ is the phase function computed as:

$$\Theta(\Phi) = \frac{2}{3\pi^2}\left[(\pi - \Phi)\ \cos(\Phi) + \sin(\Phi)\right]$$

and accounts for the solar phase angle Φ (angle between the Sun-asteroid and asteroid-Earth vectors).

2.6.2 Thermal IR

For thermal IR modeling, the simulation uses either NEATM or Fast-Rotating Model (FRM). The FRM assumes fast rotating asteroids or asteroids with high thermal inertia. Temperatures using this model are constant along the equator and drop toward the poles. The NEATM model also incorporates a beaming parameter, η, to account variations in the asteroid's spin rate, thermal inertia, and surface characteristics (roughness). Generally, this beaming parameter is produced as a fit to spectral data. For the purposes of this simulation, the simulated asteroid catalog has the beaming parameter drawn from a fit to beaming parameters as computed using data from the NEOWISE project, which catalogued 436 NEOs with sufficient spectral information to compute a beaming parameter. The fit used was log-normal distributed with $\mu = 0.4242$ and $\sigma = 0.3374$. The value for beaming was truncated to the range between 0.753 and π, which are the highest (corresponding to the limit where NEATM and FRM are equivalent) and lowest from the NEOWISE database. Another important term in the thermal model is the solar phase angle, which affects the temperature distribution of the projected area of the asteroid surface.

Ultimately, using either model yielded similar results, when looking at overall cataloging performance of the sensor systems.

2.7 Population Modeling

Simulating the survey cataloging capability requires an accurate model of the population of objects. Some objects are more difficult to find than others due to their orbit, albedo, or size, and the relative difficulty depends on the survey methods. A bias in the population could lead to simulation results that erroneously favor one survey type over another. The problem is complicated by incomplete knowledge of the real population: the known population is biased toward objects that are easier to find using existing surveys. For this simulation the best de-biased data and models available were used. Orbital elements were drawn from the de-biased near-Earth object model of Granvik [Granvik et al. 2016]. Object size and geometric albedo were taken from the SDT 2017 report. The thermal beaming parameters, important for infrared emission, were taken from the NEOWISE database [Mainzer et al. 2016]. In order to test whether the rotation of non-spherical asteroids and the corresponding change in apparent size would affect the survey, spin rates and lightcurve magnitudes were drawn from the lightcurve database [Warner et al. 2009].

To make the population modeling flexible, all aspects of the model were encoded statistically, and individual test populations were created by statistical draws. The orbit semi-major axis, eccentricity, and inclination were drawn together from the Granvik model bins, and distributed uniformly within the bin. All other parameters, including the other three orbital elements, were drawn independently of each other. For the potentially hazardous object (PHO) populations, a set of orbits were drawn from the Granvik near-Earth object (NEO) population, and then all non-PHO orbits were discarded; for purposes of this report the term PHO is used to refer to all objects with minimum Earth orbit intersection distance less than 0.05 AU, irrespective of the object size. The object sizes were drawn from a cumulative distribution function fit to the three-slope power law given in the SDT report, rather than using the SDT binned population table directly; this enforces correct size distributions within each bin, as well as simplifying the calculation of integral completeness. This is a more conservative approach than SDT. Geometric albedo was drawn from a bimodal distribution fit to the histogram given in the SDT report. The visible light reflectance was modeled using the Bowell phase function with G=0.15. Thermal modeling for the IR surveys used either the NEATM [Harris 1998] or FRM [Lebovsky and Spencer 1989] model; for the NEATM model, the beaming parameter was drawn from a log-normal distribution fit to the NEOWISE database. The thermal emissivity of all objects was assumed to be 0.9. Each population drawn from these models is expected to be statistically representative of the real population and provide an unbiased test of the simulated surveys. Populations used were generally much larger than the real population to generate more reliable statistics.

2.8 Observation Cadences and Revisit Strategy

Observation strategies for both ground surveys and space-based platforms were developed for this study. These strategies are outlined in the following sections.

2.8.1 Ground Survey

For a ground survey, an observation approach is modeled from the Pan-STARRS strategy [Wainscoat, 2017]. The Pan-STARRS1 telescope became operational in 2010, and in April of 2014 began focusing all of its observation time on searching the sky for NEOs.

Sky Sampling

Before describing a pointing strategy, the available portion of sky to be surveyed is first defined. The region of sky to be surveyed covers the full range of Right Ascension, and minimum and maximum ecliptic declinations, $[\delta_{min}, \delta_{max}]$, are specified to allow limits on the search space. A grid of points is then specified over this desired region of the sky. Declination grid spacing is defined equal to the instrument FOV, and Right Ascension grid spacing is scaled by the cosine of the declination for each node. The sky is also subdivided into blocks, analogous to the “chunks” employed in the Pan-STARRS strategy. A block specifies a smaller range of Right Ascension and declination. For Pan-STARRS, this corresponded to 1 hour of Right Ascension and a variable span of declination ranging from 8-32°. The block sizing is parameterized for this study so that it may be easily adjusted. For each block, some subset of the grid points falls within the block.

Exclusion Regions for Ground Surveys

To limit observations to night-time only, a maximum Sun elevation angle (ϕ) is specified. In addition, a minimum elevation angle (ϵ) is defined for each observation to avoid obstructions along the horizon. Only those regions of sky that satisfy these elevation constraints are observed. Several exclusion regions are defined that allow avoidance of bright regions of sky. A Moon avoidance angle (α) is specified, and the region of sky within this angle of the Moon from the observer is excluded from the search. The galactic plane is also excluded by defining an angle (β), and no observations are taken within an angular displacement of β from the galactic plane. These angles are represented in ***Figure 4.***

In addition to regions of sky that are excluded at each instant of the search, nights of zero-visibility due to weather are modeled. A clear sky probability is defined as the average over the monthly average clear sky ratio data provided for the Subaru telescope (https://www.naoj.org/Observing/Telescope/ImageQuality/Seeing/). For a search simulation over some number of nights, bad weather nights are randomly generated based on the clear sky probability, and no observations are taken on these nights.

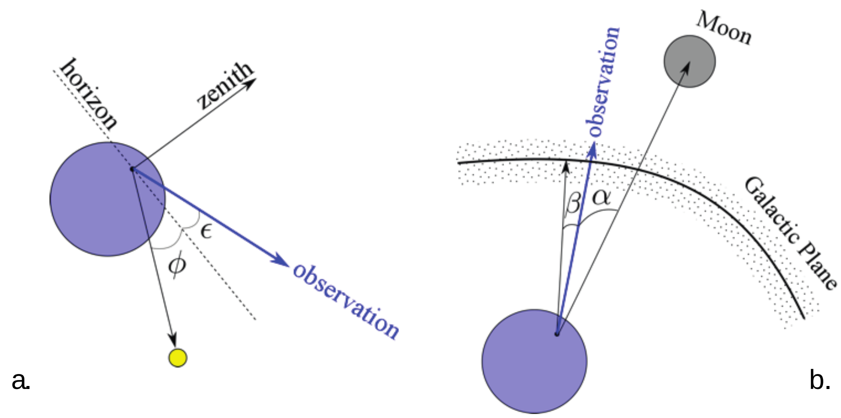

Figure 4 *(a) Defining maximum Sun elevation angle, and minimum observation elevation angle, (b) Defining exclusion regions in the vicinity of the Moon and the galactic plane*

Search Strategy

The search begins by scanning one block, where the first block is selected randomly from the set of blocks that encompass the station zenith Right Ascension. To scan a block means that the grid points within that block are observed, where the scanning occurs in a raster pattern. Each grid point is observed for some number of seconds, and this duration is a constant value specified at the start of the search. Once the first block is selected, a "block list" is formed, so that scanning the blocks in the order of the block lists yields a raster search pattern. An example sky gridding, and block spacing (similar to the Pan-STARRS chunks) is shown in ***Figure 5.*** The blocks are numbered and their delineation is shown with the vertical and horizontal lines, with grid points plotted as blue dots. Missing grid points have been excluded based on a 10° galactic plane avoidance angle. The red arrows show the raster pattern for a sequence of observations along a block list, as well as for the individual scans of a block.

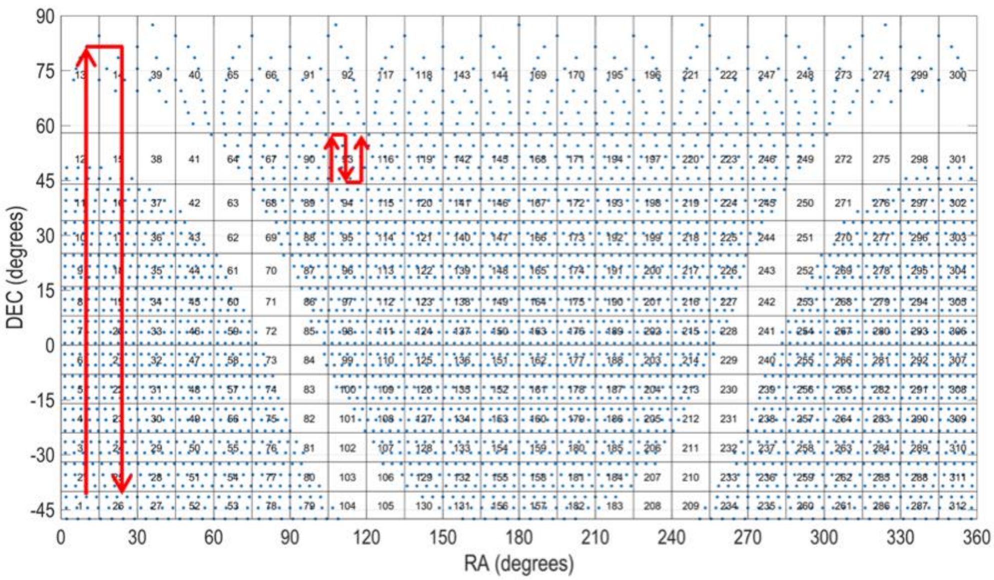

Figure 5 *Example Pan-STARRS-like sky sampling pattern*

To control the revisit cadence for a particular point in the sky, each block in the list is scanned M times before proceeding to the next block. A set of M scans of a particular block results in a tracklet. For a particular night, this pattern is followed resulting in a series of tracklets corresponding to some subset of blocks from the block list. On the next night of observations, the search resumes with the last scanned block from the previous night. After N nights, the search resets to the first block from the block list. This allows for acquisition of a series of tracklets, each spaced N nights apart. A third counter, P, allows the number of tracklets to be limited to the number that is required for sufficiently accurate orbit determination. Once a block is observed P times, it is moved to the end of the block list, thus yielding P tracklets (each consisting of M observations of a block) spaced N nights apart.

Example Search Simulation

An example Pan-STARRS-like survey was performed for comparison. Here, the telescope is placed at a latitude of 20.8°, and the region of sky is limited to the declination range $[\delta_{min}, \delta_{max}]$ = [-47.5, 90]°. A maximum Sun elevation angle of ϕ = -18° is defined, in addition to a minimum elevation angle for observations of ϵ = 10°. The exclusion region around the Moon is defined by $\alpha = 5°$ (new to quarter Moon), and α = 25° (quarter to full Moon). The galactic plane avoidance angle is set to β = 10°. Revisit cadences are specified by M = 4, N = 1, and P = 3. The results of a 920-day search simulation are represented in ***Figure 6***, where each grid point is colored by number of visits during the full simulation. Because the Moon occupies declination values nearer to 0°, the blocks near the ecliptic generally have fewer visits. Regions with zero visits, colored in black, never satisfy the minimum elevation angle constraint. The white region with no grid points is the region of exclusion around the galactic plane.

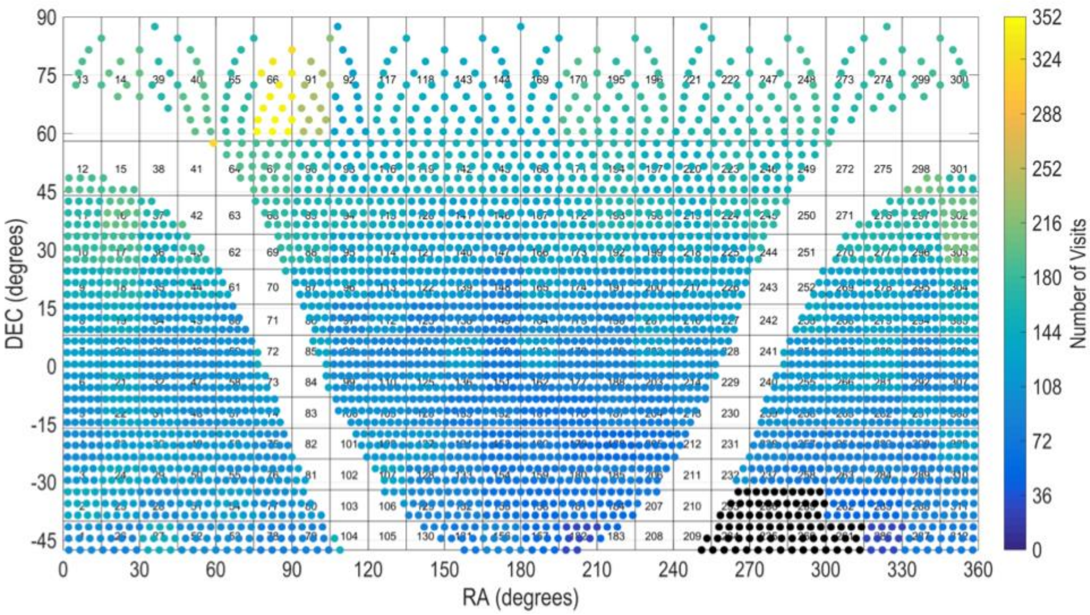

Figure 6 *Results of an example Pan-STARRS-like search simulation over 920 days*

2.8.2 Space-Based Survey – Earth Orbit

For an Earth-orbiting platform, a search strategy is employed that uses the same sky scan sequence and revisit logic as the ground survey strategy described in the previous section. The sky sampling and search strategy are identical to those described for the ground survey. The difference between the Earth-orbiting platform search and the ground survey is in the definition of exclusion regions.

Exclusion Regions for Earth-Orbiting Platforms

Possible sources of stray light for an Earth-orbiting platform include the Sun, Earth, Moon, and galactic plane. The Moon and galactic plane avoidance regions are again defined by angles α, β, respectively. An Earth avoidance angle (γ) is also defined, and no observations are taken within regions of sky where any of these avoidance constraints are violated.

In addition to avoiding looking too close to the Sun, it is useful to define a maximum solar elongation angle to reduce the search space and focus on areas where higher NEO populations are expected. To enable both goals, a range of solar elongation angles [φ_{min}, φ_{max}] is specified and only observations within this elongation window are taken. The angles defining the Earth-orbiting platform exclusion regions are shown in ***Figure 7***.

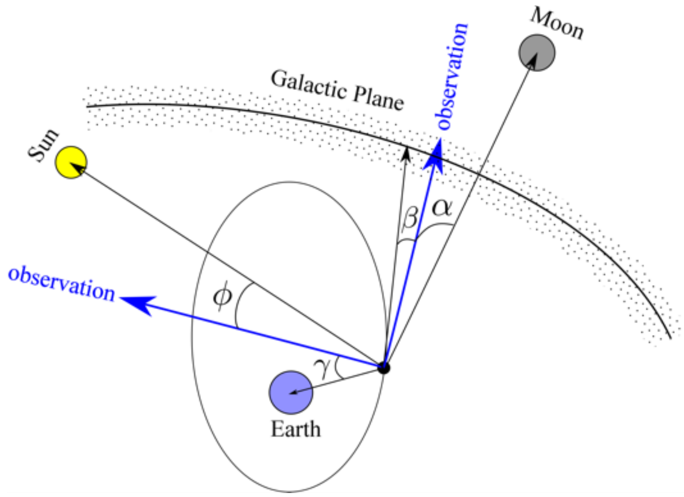

Figure 7 Defining exclusion regions for the Sun, Moon, Earth, and galactic plane

2.8.3 Space-Based Survey – Sun-Earth L1 Orbit

An observatory in the vicinity of the Sun-Earth L_1 point offers distinct geometrical features from the perspective of an observation strategy. For this study, a search strategy and revisit cadence for such an observatory is modeled after that employed by Mainzer [Mainzer et al., 2015].

Sky Sampling

As with the ground and Earth-orbiting platforms, the region of sky to be surveyed covers the full range of Right Ascension, and a declination range [δ_{min}, δ_{max}] is specified at the start of the search. In addition, the desired solar elongation range [φ_{min}, φ_{max}] is set, and all observations occur within this region. The accessible regions of sky are represented as the white cones in ***Figure 8(a).*** The Sun and Earth are plotted in yellow and blue, respectively. The L_1 point is at the vertex of the white cones.

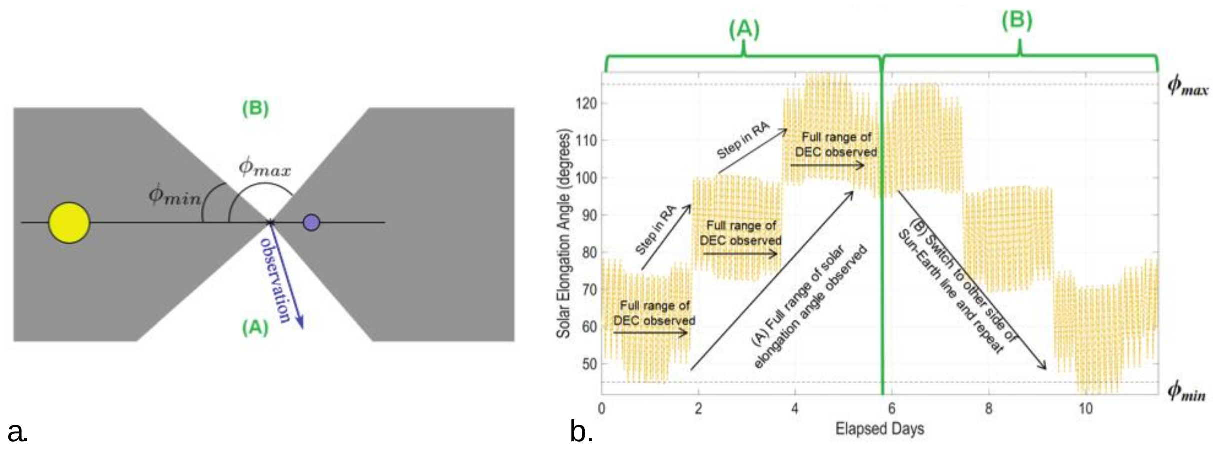

Figure 8 (a) Defining desired solar elongation range for observations, (b) Example search sequence

Search Strategy

For an L_1 observatory, a block is defined as n x m pointings (Right Ascension x declination), where the distance between pointings is defined by the instrument FOV. A block is scanned M times before proceeding to the next block, defined as a step in declination by m*FOV. This is repeated until the full range of declination is observed. A step in Right Ascension of n*FOV is then taken, in addition to returning to the minimum declination block, and observations resume until the full solar elongation range has been observed. This strategy is then repeated on the opposite side of the Sun-Earth line, so that the full range of solar elongation is sampled. An example of a search sequence is plotted in ***Figure 8 (b).***

2.9 Backgrounds

A major challenge in detecting small objects in the solar system is picking them out from a bright and cluttered background. Stars, planets, and more distant asteroids clutter the sky; however, these can be eliminated from consideration by their low rate of motion compared to NEOs, and are not included in the simulation. A diffuse background also exists due to the thermal emission and scattered sunlight from a cloud of dust in the inner solar system, the zodiacal cloud. This zodiacal background can pose significant problems, adding to the noise in the system and saturating the detector if the integration time is too long. The background is modeled using the IPAC model ["Background Model"], which is fit to COBE/DIRBE data [Wright 1998, Gorjian et al. 2000]. Data from the IPAC is integrated over each sensor's wavelength band, and implemented in the model as a lookup table over look direction and time of the year.

Ground sensors, needed to generate a baseline catalog, face additional challenges due to the atmosphere. Although the surveys avoid looking at or near the moon, moonlight scattered through the atmosphere adds to the background light. The simulation uses a moonlight model that depends on the look direction, moon elevation, and phase [Krisciunas and Schaeffer 1991]. Ground sensors also lose nights due to cloud cover; this is implemented by a random draw, using the historical probability of cloudy nights at the Subaru telescope ["Seeing"]. Subaru telescope data was also used for the atmospheric seeing: turbulence in the atmosphere causes images to be blurred, reducing the fraction of light intercepted by the brightest pixel on the detector.

2.10 Model Results

The following figures provide model results for various cases considered as part of this effort. As previously mentioned, one of the main outputs of the analysis phase of the simulation is catalog completeness: how well do the sensor systems in question catalog the synthetic population? The answer to this question then provides an estimate of real-world performance by looking the statistics of cataloging large synthetic populations.

The results shown are, unless otherwise noted, run for a PHA-only population, in keeping with the SDT results. That is a more conservative approach, as results run with the full NEO catalog are generally more favorable. Also, the output is for integral completeness: completeness values are computed within asteroid size bins, and each point represents cataloging completeness for that bin and all bins with larger asteroids. The time scale for the assessment is 10 years from estimated start date of the space-based observations (2023). Both FRM and NEATM models were run for IR, and the results compare well.

Most of the cases shown here met the criteria (≥90% completeness for ≥140 m diameter asteroids) in October 2017, prior to additional validation with SDT and GSFC. An error was discovered in the background, where the input into the model was ~2 orders of magnitude dimmer than the background that should be expected. The results shown here have been corrected to include the brighter background, however the cases no longer achieve the desired goal. However, they do demonstrate what can be achieved with the less expensive options. Additionally, they also show that it is possible to phase out the “detection and tracking” and “characterization”, where the “detection” is done by a larger Visible system (>1 m) and the follow on “characterization” can be performed by a smaller IR system.

In the following sections, Long Wavelength Infrared band (LWIR) refers to 6-7.5 μm, and Medium Wavelength Infrared band (MWIR) is 4-6 μm. Additional cases were run with the longer wavelength band 6-10 μm as well, for comparison with the SDT results for the 0.5 m IR telescope.

2.10.1 Baseline

The “baseline” results are cataloging performance for a baseline architecture which includes existing and planned ground sensor NEO observation platforms, out to 2033. The ground baseline started June 1, 2001 with a LINEAR-like system, with a 1 m aperture telescope. In June 2007, it increased the aperture size to 1.5 m, and in June 2012 it increased the aperture to 2m. The baseline is run out to middle of 2023, and is shown in ***Figure 9*** with the SDT baseline. In early 2023, an 8-m ground visible telescope comes online and adds to the existing assets.

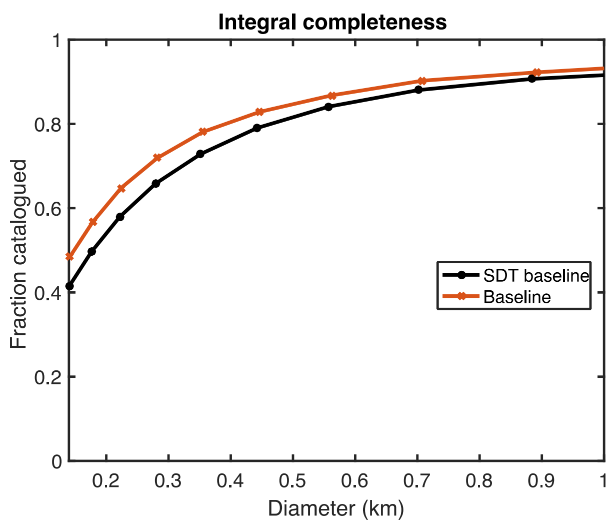

Figure 9 *Ground baseline run out to 2033. JHU/APL model includes an additional 8-m Ground Based Observatory coming online in 2023.*

The two results agree well, especially given the different simulation methodologies used. The “Baseline” data will be repeated in the following charts to provide better context for the other results shown, as the calculated completeness metrics also include baseline-catalogued objects.

2.10.2 Cases of Interest: Detection and Tracking

Figure 10 and ***Figure 11*** show the set of results for cases of interest for detection and tracking. “Lorrimod” refers to a modification of the LORRI sensor used on New Horizons, and is a 2.8° x 3.4° field-of-view system, with 3 CIS113 CMOS detectors abutted and a 40 cm aperture (case 3c).

The quad sensors are similar in design, but are four telescope assemblies and four sets of detectors on one platform, abutted to effectively create a system with 4 times the field of view (similar to TESS). A system for ISS is also shown. None of the cases met the study goal, however they demonstrated what can be achieved with a less expensive options.

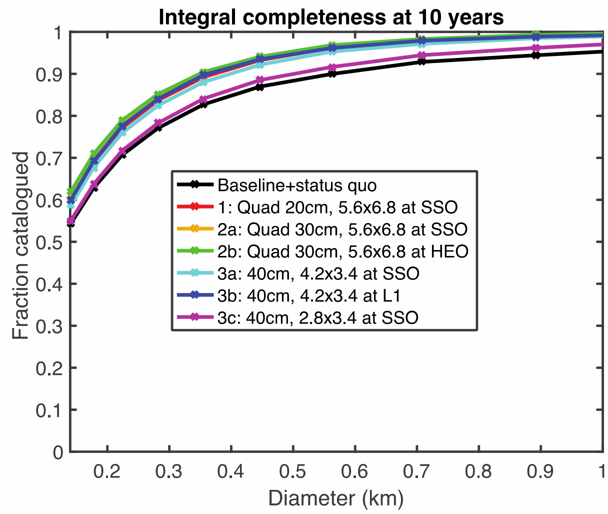

Figure 10 *Cases of interest for the AoA study. SSO – Sun Sync orbit; L1 – Halo orbit around L1 point*

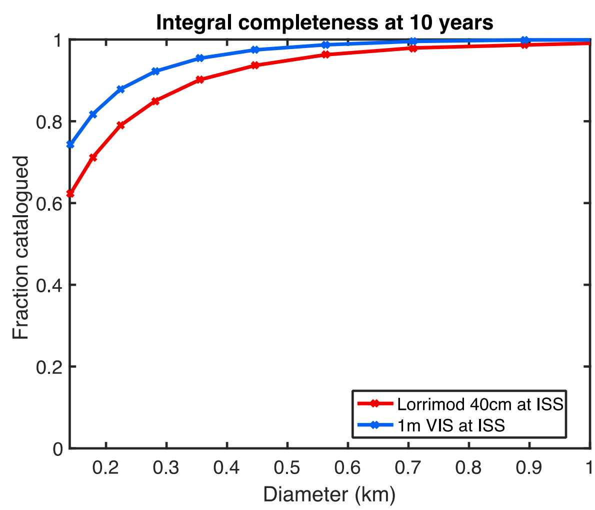

Figure 11 *Results for the International Space Station. A 1m Visible telescope is assumed to be at the limit of a reasonable size gimbal platform to take out the jitter and improve the pointing stability for the Space Station case.*

2.10.3 Cases of interest: IR 20 cm System, MWIR and LWIR for characterization

One of the key interests of this study was to explore separating detecting and tracking of the NEOs and the characterization. The team assumed that the detection and tracking would be done by a visible system, and investigated characterization via smaller IR telescope. Characterization required two IR bands to get two temperatures on the black body curve to retrieve the size of the asteroid. ***Figure 12*** shows a fraction of the "catalogued" asteroids characterized in 10 years by a small hosted IR sensor. In this case, the sensor was a 0.2 m hosted IR telescope in the GEO orbit, described in ***Section 3.1***. Longer integration times decrease the amount of sky covered, and therefore perform worse despite the increased sensitivity. The case shown here uses a narrow band for LWIR (6-7.5 μm) and can be further improved with using a different IR detector that covers 6-10 μm.

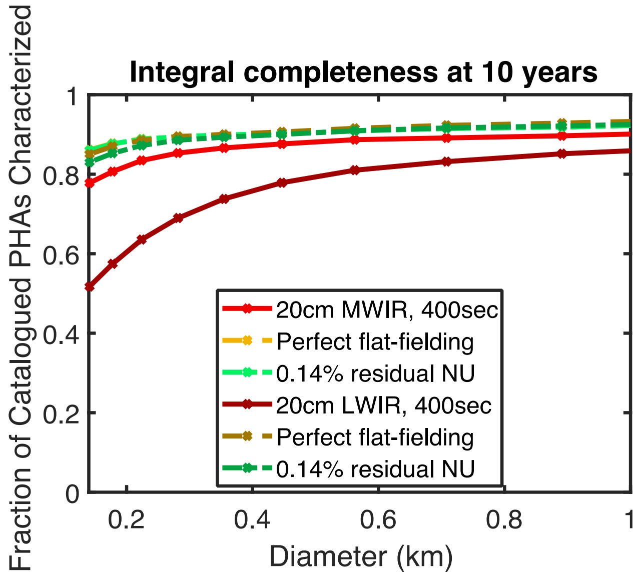

Figure 12 Fraction of the catalogued PHAs characterized by a 20 cm IR sensor for a variety non-uniformity residuals (2%, 0.14% (based on WISE data), and 0%). Demonstrates the need for flat fielding on orbit.

2.10.4 Synthetic Tracking System in CubeSats

AoA simulation was used to evaluate a CubeSat concept with synthetic tracking (velocity match filter) based on Shao et al. [Shao et al., 2017], as shown in ***Figure 13***. A constellation of CubeSats in L1 orbit was assumed with > 6 CubeSats that would meet the required revisit rate specified in SDT report. The sensors were 10 cm visible telescopes (the largest current size for CubeSat accommodation) that had 800 s integration times by co-adding 80 images onboard. Based on current flight attitude system control performance from RAVAN and MinXXS using BCT XACT system, achievable pointing performance is >15-20" over 10 seconds, consistent with Shao et al. It was found that better attitude control and/or bigger aperture was needed for 90% completeness, even with synthetic tracking. Other issues included the large data volume. If a CubeSat can downlink 227 GByte/day, then no processing onboard was needed. If a "Shift and add" technique was used, it reduced it to ~3 GBytes/ day. These communication links are beyond current CubeSat capability. Advancement in matched filter algorithms could potentially reduce data volume further, but survey of current algorithms did not change conclusion.

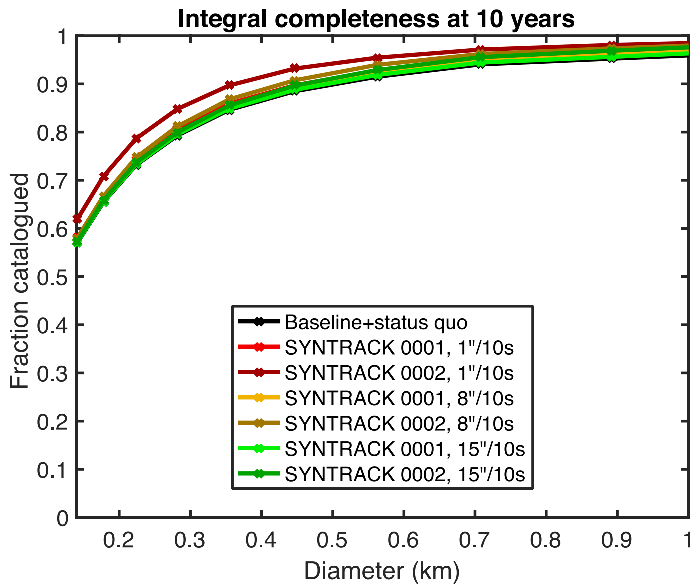

Figure 13 *Results for 10 cm Vis systems with synthetic tracking. Two syntrack cases represent different declination ranges: 0001 was ± 26°, and 0002 ± 15°. The jitter in both cases was varied 1", 8" and 15" over 10 sec integration time.*

2.11 Comparison with SDT

Although in many respects this effort followed the example set by the SDT report, some differences between the two models exist. Where the SDT report uses two different model frameworks for visible and IR telescopes, the JHU/APL simulation is unified. This led to AoA testing 'sweet spot'-focused survey strategies for visible as well as IR telescopes, whereas the SDT visible surveys included opposition in cases it was not obscured by Earth or Moon. The JHU/APL simulation also uses a test population with a size distribution proportional to the real population, rather than the SDT's approach of equally filled logarithmic size bins. Both models use a zodiacal background that depends on the pointing direction, but different, albeit numerically similar, models are used. There are also slight differences in the detection calculation: JHU/APL uses a sharp SNR threshold while SDT uses a smooth function, and JHU/APL's point-spread function accounts for trailing while the two effects are handled separately in the SDT model. The SDT thermal model is in good agreement with both NEATM and FRM, and since AoA NEATM and FRM runs agreed well with each other.

The differences between the two models lead to JHU/APL's cataloging completeness predictions being somewhat more pessimistic than SDT's for visible surveys and for IR surveys*. **Figure 14*** and ***Figure 15*** illustrate the differences for Visible and IR systems. The visible system was then further validated with the GSFC results, however no validation of IR model was done and small differences remain.

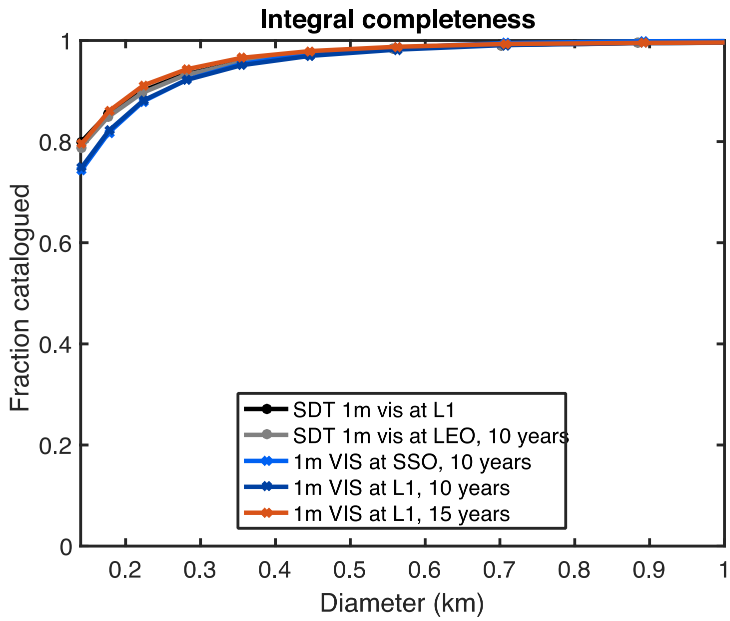

Figure 14 *Comparison of JHU/APL results with SDT results for 1m VIS telescope*

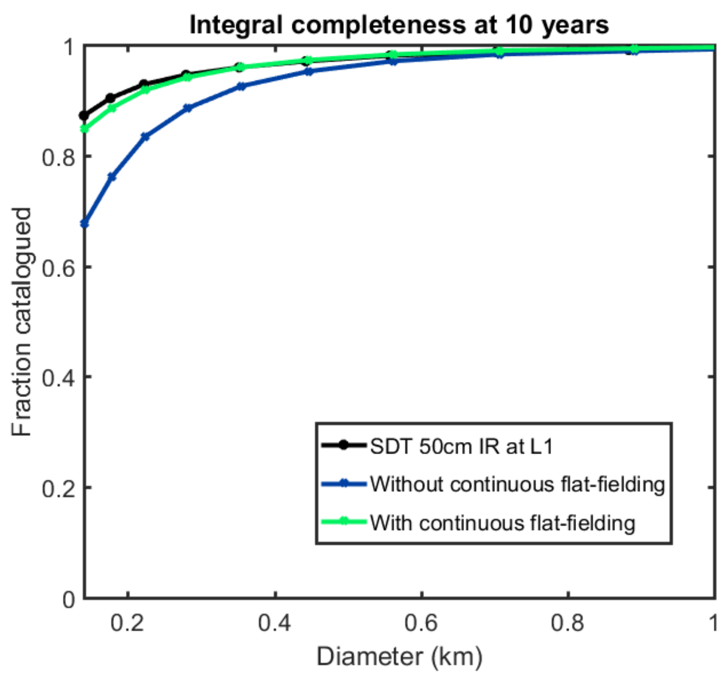

Figure 15 *Comparison of JHU/APL results with SDT results for 0.5 m IR telescope at L1*

2.12 Comparison with GSFC

A detailed comparison was conducted with the space-based visible-light survey simulation tool developed at GSFC to build confidence in the model. In addition to a top-level comparison of the cataloging performance of a particular survey concept, individual components of each model were compared to identify discrepancies. Several differences exist in the two modeling approaches and the assumptions made that result in differences in the predicted catalog completeness. Issues with both models were also found and corrected during the comparison campaign.

The comparison case, shown in ***Figure 16***, used a 40cm visible telescope situated at the Sun-Earth L1 point. Both models used the same PHO population, the same observation schedule, and the same telescope properties. Because GSFC does not have a ground-based telescope model, the baseline ground-based survey catalog was modeled with the JHU/APL tool, and these baseline results were used for both models. A major difference is that the JHU/APL model lets the zodiacal background vary with look direction, while GSFC uses a single background value. The JHU/APL tool calculates the signal in the brightest pixel statistically, while GSFC calculates the location of the image center within the pixel directly, leading to small differences in the point-spread function and trailing losses. Finally, differences remain in the calculation of the signal-to-noise ratio, due to different assumptions about co-added frames and how trailing is handled, and the detection threshold. These differences contribute to a more pessimistic catalog completeness result from GSFC than from JHU/APL for the comparison case. Although JHU/APL's model does not exactly match SDT's or GSFC's, the fact that JHU/APL's results fall between those of the two other models builds confidence in the JHU/APL model.

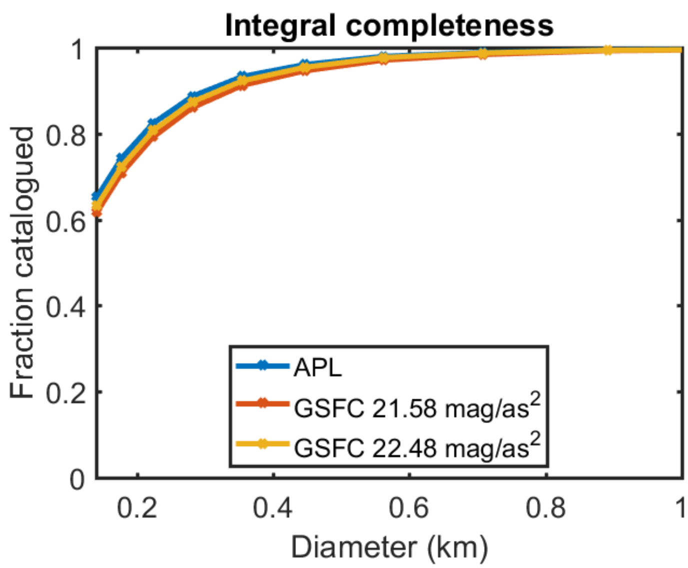

Figure 16: *Comparison of JHU/APL NEO Simulation and GSFC simulation results for a 40-cm visible telescope at L1. All results use the same PHO population with the same baseline catalog completeness before survey start. The JHU/APL results use theJHU/ APL model, including pointing-dependent zodiacal background. The two GSFC results use a single, pointing-independent background, and the simulations differ in whether the value used is the median of the pointing-dependent backgrounds JHU/APL samples (21.58 magnitudes per square arcsec), or GSFC's preferred, dimmer value (22.48 mag/as^2). Results are quite comparable, with GSFC's model more pessimistic than JHU/APL's for both background assumptions.*

3. Payload Overview

Table 1 *Summary of the Alternative Cases*

Detect and Track	*Characterize*

	Case 1	Case 2a	Case 2b	Case 3a	Case 3b	Case 3c	Case 5
Payload	0.2m VIS Quad	0.3m VIS Quad		0.4m VIS			0.2m IR
Payload FOV	5.6°×6.8°* (2.8° × 3.4°/ tlscp)			4.2°×3.4°		2.8°×3.4°	1.7°×1.7°
Detectors	2 abutted E2V CMOS			3 abutted E2V CMOS		2 abutted E2V CMOS	RVS HgCdTe, MWIR & LWIR, Microlens Array
P. Mass/Power	50kg/45W MEV	127kg / 45W MEV		64kg / 19W MEV		64kg / 19W MEV	228kg/461W MEV
Data Volume in Day/ Processing	38 GByte/ co-add images	47 GByte/ co-add images		14 GByte/ co-add images		15 GByte/ co-add images	0.82 GByte/ no on-board processing
Orbit/ ΔV/ C3	SSO, 700 km, Dusk-Dawn/ 104 m/s		HEO, 2:1 Lunar Resonant, 237 m/s/ -2.8 km^2/s^2	SSO, 700 km, Dusk-Dawn/ 104 m/s	L1 Halo /106 m/s/ -0.61 km^2/s^2	SSO, 700 km, Dusk-Dawn/ 104 m/s	GEO, ~2400 m/s
Launch Vehicle	Taurus 3210**		Antares 232**	Taurus 3210**	Antares232**	Taurus 3210	Depends on host
Lifetime/ Class	10-year / B						2 year / D
Bus Architect.	Dual String						Single String
Bus Description	3-axis					NSTP-Sat, spinner	Hosted, 3-axis
Bus Mass (kg) /Power (W) MEV	249 kg dry/ 232 W	378 kg dry/ 245 W	412 kg dry/ 252 W	280 kg dry/ 205 W	302 kg dry/ 307 W	*Need more info, ~1500 kg*	*Need more info*
Bus Comms	1W X-band down; 0.5W S-band up, downlinks to McMurdo, SSC North Pole, KSAT Svalbard & SSC Kiruna		2.5W Ka-band down, S-band up, downlink to White Sands 18m	Same as Case 1&2a		Same as Case 1&2a	*Need more info*
Bus Attitude Control	Reaction wheel & thruster (1lbf); sun and fine guidance sensors (FGS), MIMUs					FSM, FGS, de-spun platform	*Pay includes gimbal, wheels*
Bus Propulsion/ Avionics	Chemical, monoprop/ Dual IEM with 2 Single Board Computers (one for Attitude Control processing only)						Dual Mode

A number of optical payload variants were considered to meet the challenging requirements of high sensitivity, wide field-of-view, spectral band, and cost. The downselected payloads that were analyzed in detail in this study are summarized in ***Table 1***.

3.1 Sensors

Two primary instrument designs were considered to fully address the observation requirements: A visible, wide-angle system to detect and track the solar illuminated NEOs, and a MWIR narrow-angle system to characterize the NEOs from their thermal emission.

The visible imaging systems leveraged a passively cooled CMOS large area array made by E2V. A single CMOS detector array is 4608×1920 pixels and is designed to be abutted with very small dead space between detectors, permitting the various fields-of-view analyzed in this study. As shown in ***Table 1***, this study considered the cases of abutting two and three CIS113 CMOS detectors. The large 16-µm square pixels and low noise detector matched the optical performance of the telescope designs for the visible system. Two unique telescope designs were considered: (1) A low-cost Ritchey-Chretien designed scaled from the 0.2m *New Horizons*/Long Range Reconnaissance Imager (LORRI); and (2) A compact TMA with an optional fast steering mirror to reduce jitter. The latter design with the FSM was optimized to be integrated on the NASA Science/Technology Platform Satellite (NSTP-Sat) with a despun platform.

A modified version of NH/LORRI telescope design was considered for Case 1 with a 2.8°×3.4° FOV, replicated four times with each telescope angle for a large effective FOV of 5.6°×6.8°. Each 0.2-m aperture telescope used two abutted E2V CMOS detectors. The smaller 0.2-m optics reduces complexity of fabrication, and because the design of all four camera systems is identical, the overall system cost is reduced**.** ***Figure 17a*** and ***b*** show a single CIS113 CMOS detector and Ritchey-Chretien telescope system. ***Figure 17c*** depicts the notional quad-camera design to accommodate the very large FOV required.

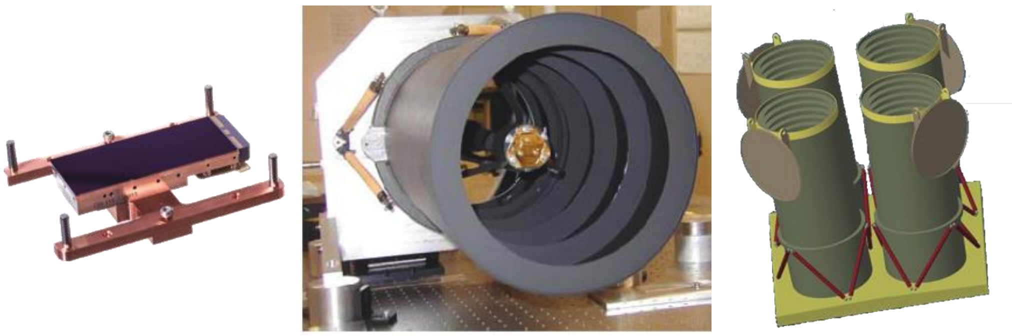

a. b. c.

Figure 17 (a) Single E2V CIS113 CMOS Detector, (b) Single LORRI-like telescope, (c) Notional Quad System

The second design was used in Cases 2a and 2b and was largely the same visible camera design as described for Case 1, however, the effective aperture of each of the four telescopes was increased to 0.3m. This modification increased the overall cost of the system slightly, but improves the overall sensitivity by more than a factor of two.

The visible detection and tracking system designed for Cases 3a and 3b, increased the effective aperture of the Ritchey-Chretien telescope to 0.4m, and a third CMOS detector was added to the focal plane to increase the full FOV to 4.2°×3.4° and array size of 1920 × 4608 pixels.

The alternate telescope considered, a compact TMA design provided flexibility in the placement of the optical components to incorporate a fast-steering mirror (FSM). The FSM provides jitter control 175 µrad which is more than sufficient for this system to be used with the NSTP-Sat bus with a despun platform, as shown in ***Figure 18***.

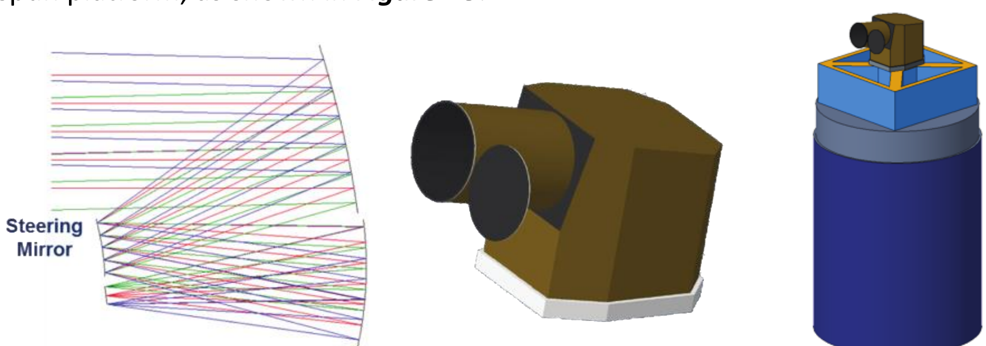

a. b. c.

Figure 18 *(a) Compact Three Mirror Anastigmat (TMA) ray trace with FSM, (b) TMA telescope, (c) Notional accommodation*

The purpose of the visible detect and track camera was to provide the location of NEOs to sufficient accuracy that the two-band MWIR and LWIR Optical Payload with a much narrow FOV (1.7°×1.7°) on a two-axis gimbal can be directed to in the sky for longer stares. The 0.2-m effective aperture reduced the overall cost and required resources of the system.

The IR Optical Payload consisted of a 20-cm TMA design on a gimbal. The design heavily leveraged a previous study in which the size-weight-and-power (SWaP) was optimized for a particular spacecraft. The actively cooled mercury cadmium detectors were integrated onto a high-performance ROIC made by Raytheon Vision Systems, the RVS SB463, developed on another JHU/APL program. The 18-µm pitch pixels were diffraction limited with the 0.2-m telescope. To mitigate this, an array of silicon microspheres was mounted in front of the MCT detectors matching the size of the Airy disk at 5.5 µm in the MWIR channel, and 7.5 µm in the LWIR channel. This effectively reduced the spatial resolution by a factor of 3.5 in the MWIR band and 5 in the LWIR band, but the critical contribution of the IR characterization telescope was to measure the NEOs emission in two bands to determine its temperature and thereby infer its size and mass. The high precision tracking information in which the spatial resolution was required was provided by the visible telescope.

Figure 19 shows the RVS MCT detector mounted on the SB463 ROIC, a cartoon of the gimbal and IR telescope, and a representative microlens array.

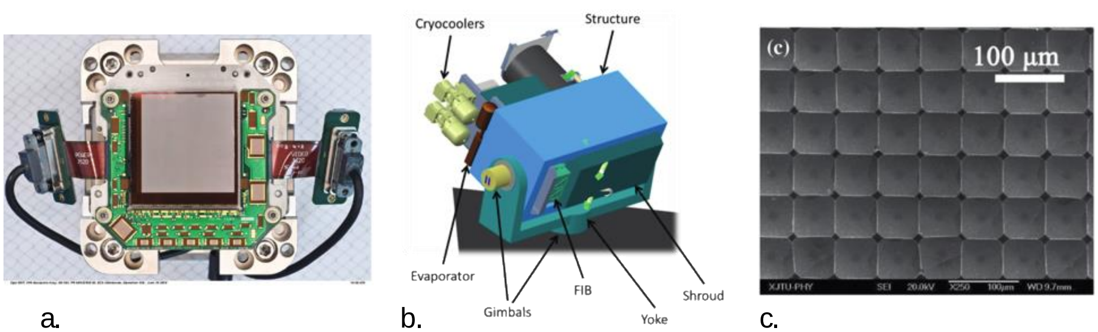

Figure 19*. (a) 2k×2k MCT FPA, (b) IR Telescope, (c) Microlens array.*

3.2 Data Processing Units

Following sections describe the DPUs used with the payload.

3.2.1 Detect and Track Data Processing Unit (TDPU)

The Detect and Track Data Processing Unit (TDPU) was used with the visible tracking telescope. The TDPU design is a legacy component common to nearly all recent flight sensors built at JHU/APL. This unit was based on the Parker Solar Probe WISPR instrument and consisted of four or five boards depending on whether a two or three detector configuration was used. The overall dimensions of the stacked configuration are 212 mm × 75 mm × 116 mm (4-boards). The baseline is the four-board configuration: a processor board, a low-voltage power supply (LVPS) board, and two imager/memory boards. The maximum expected mass was 1.74 kg.

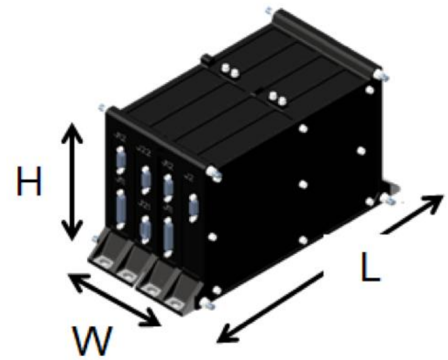

__Figure 20.__ Data Processing Unit (L = 0.212 m, W= 0.075 m, H= 0.116 m)

The DPU took full advantage of all the recent developments in the evolution of the JHU/APL DPUs, especially the improved packaging used in Parker Solar Probe flight-qualified chassis slice design, and recent developments implemented on the Europa Mission's MISE instrument. The microprocessor system on the processor board controls all the camera functions and the pixel processing pipeline. A Field-Programmable Gate Array (FPGA, RTAX2000SL) hosts a 16-bit microprocessor that responds to SV commands, collects and transmits telemetry, and configures the focal plane electronics for the desired operating mode. Rad-hard MRAM and SRAM support processor operation. The LVPS board receives primary SV power and generates secondary power for the DPU (unswitched), and power for the focal plane electronics. The imager memory board provides additional capabilities and image storage for implementation of more advanced image processing algorithms, or buffering before the image data may be telemetered.

The instrument flight software built on common flight software flown on many JHU/APL missions. It executes on a 16-bit SCalable Instrument Processor (SCIP) microprocessor in the DPU Processor Board FPGA, providing telemetry and command handling. Efficient, macro-based CRISM-heritage observation control executes image sequencing using three commands: define observation-specific parameters and values; load a string of stored macro IDs with time delay parameters; initiate macro sequence execution. There are ample memory resources for the visible camera macro command library.

3.2.2 IR Characterization Sensor DPU (IDPU)

The overall structure of the IDPU was very much the same as the TDPU, with the addition of an interface card that can used to communicate with the cryocooler control electronics (CCE). The CCE is a stand-alone fully qualified electronics box for providing temperature control of the two-pulse tube cryocoolers. The SCIP processor adequately address all the onboard processing needs.

4.0 Spacecraft and Launch Vehicle

For most cases identified in ***Table 1***, a preliminary spacecraft design was produced to accommodate the notional payload described above. The launch vehicle was then selected based on the C3 needed to reach the desired orbit and the mass of the space vehicle (see **Appendix B** for mass summary details and launch vehicle selection). Case 3c uses the NASA Science/ Technology Platform Satellite (NSTP-Sat). Case 5, which is a small IR telescope, is a hosted payload. All of the spacecraft buses were dual-string, had a design lifetime of 10 years, and were mostly 3-axis stabilized (other than NSTP-Sat, which presented its own unique challenges). The amount of propellant varied based on the orbit they were trying to reach. For attitude control they all used reaction wheels, thrusters, and fine guidance sensors (FGS) to meet stringent payload pointing and knowledge requirements. Inclusion of FGS meant that more avionics processing power was allocated to closed loop attitude control solutions, and required an addition of another processing card. All of the components were at TRL 6 or greater, and based on heritage spacecraft buses. Communications approaches varied based on the amount of data needed to be downlinked and observation strategy. Additional unique features of the examined case are summarized below.

Case 3c: NSTP-Sat

The NSTP-Sat is a spacecraft platform available to NASA as excess Government property through interagency agreement. It can be launched on NASA procured launch service or on the Space Launch System Exploration Mission-2 launch as a co-manifested payload. The size of its propulsion and comms accommodates possible launch to LEO (preferred option), MEO, GEO, or L1. NASA solicited RFIs in March 2017 to understand use possibilities for this platform. The NSTP-Sat can launch up to 575 kg/ 1200 W payload, and support communications through Ka- and S-bands. The spacecraft was based on a Boeing GEO spinner bus, and has a despun platform. It can achieve an impressive 3 arc-sec jitter in elevation. The payload hosted on the platform is required to counteract the jitter in azimuth (in the plane of rotation), which is 20 arc-sec. The suggested payload for this bus has a fast-steering mirror.

Case 5: Accommodating 0.2 m IR hosted payload

With the hosted payload, the spacecraft bus was not designed, and it was assumed that the host handled the accommodation for the payload (e.g. mass, power, thermal). The gimballed sensor was mounted on outside of the spacecraft. To compensate for the effect of gimballed payload on the spacecraft bus attitude, payload included reaction wheels (or can also be done on a reactionless gimbal). It was also expected that the host downlinks the data from the payload, and that was included in the hosting fee.

The AoA team investigated with the Harris Corporation a possibility of hosting the payload on one of their satellites. Harris brokered a discussion with SES on possibility of hosting on a next GEO satellite. The AoA team provided high level summary of payload mass, power, volume and data requirements as well as pointing and lifetime requirements to the SES and Harris. SES came back with a WAG of $79M FY17 for hosting a 0.2m IR payload of this magnitude (incorporated into the cost models shown). Additional reduction in payload mass would significantly improve results. They also looked at 0.4m VIS version, and concluded that $37 M is realistic, and could be reduced further by decreasing the lifetime of the system to <10 years.

5.0 Mission Design

For the Earth-orbiting platform surveys, a Sun-synchronous orbit, a geostationary orbit, and a resonant orbit were investigated. In addition to these options, a Sun-Earth L1 halo orbit was also considered. Details on each of these solutions are provided in the following sections, and the summary of the orbits is shown in ***Table 2***. ΔV summary is provided in **Appendix B** for all cases of interest.

Table 2 *Summary of the mission design solutions for the study*

Orbit	Launch C3 (km^2/s^2)	Earth Altitude (km)
SSO	-56.32	700
GEO	-16.33	35786
HEO	-2.82	100,000 – 370,000
SE L1	-0.61	1.5e6

5.1 Sun-Synchronous Orbit

A representative dawn-dusk Sun-synchronous orbit (SSO) is assumed for this study. A circular orbit of altitude 700 km is assumed, with ascending node located at 06:00 LT.

5.2 Geostationary Orbit

To evaluate the performance of a representative geosynchronous orbit (GEO), an example circular, equatorial geostationary orbit is assumed for this investigation. The spacecraft is assumed to be located above -100.0° east longitude.

5.3 High-Earth Orbit

The resonant orbit used for the science phase of the Transiting Exoplanet Survey Satellite (TESS) mission provides a highly eccentric, stable orbit with a high apogee of about 59 Earth-radii (R_E), useful for taking observations far from Earth for extended durations, and with a perigee radius of about 17 R_E to allow downlink of science data at a high rate [Dichmann et al., 2014]. For this study, a similar high-Earth orbit (HEO) to that of the TESS mission was modeled, as illustrated in ***Figure 21***. The orbit is periodic in the Earth-Moon rotating frame, and is in a roughly 2:1 resonance with the Moon, meaning that after a full orbit period of the resonant solution, the Moon has traversed a half-orbit period of its orbit.

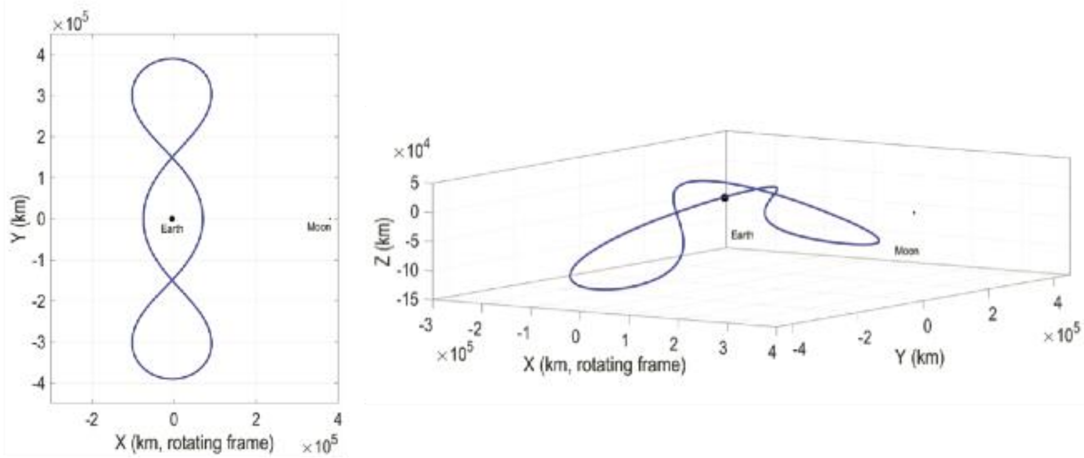

Figure 21 *2:1 resonant orbit in the Earth-Moon rotating frame*

5.4 Sun-Earth Libration Point Orbit

The Sun-Earth L_1 point provides the benefit of continuous spacecraft access, with low station-keeping costs and no eclipses. For this study, a representative L_1 halo orbit is selected, as shown in ***Figure 22***.

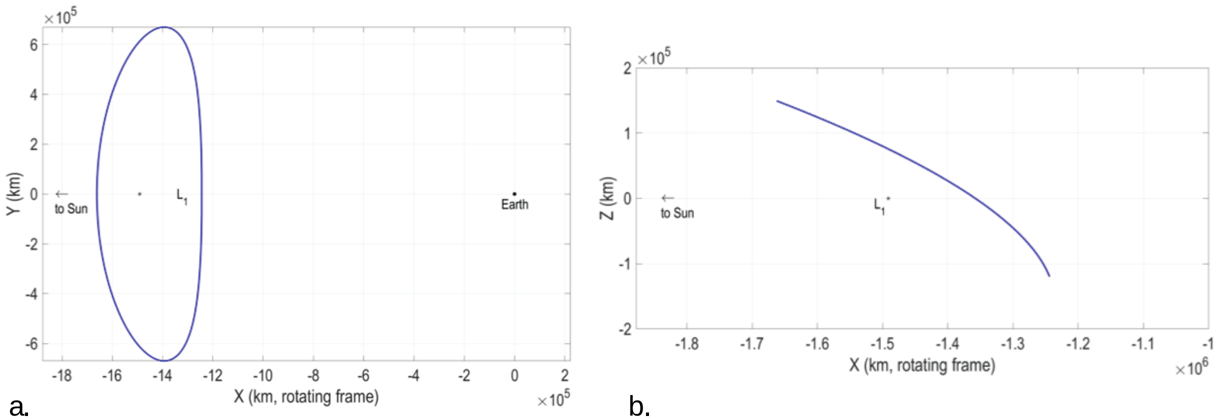

Figure 22 *L_1 Halo orbit in the Sun-Earth rotating frame (a) X-Y view, (b) X-Z view*

6.0 Mission Cost

One of the major considerations in determining the most appropriate means of detecting NEOs is the cost of the observatories dedicated to the mission. To identify the most affordable options, this study estimated the life-cycle costs of various space-based observatory options.

This study relied on parametric cost-estimating relationships (CERs) to estimate the design and development cost of each mission considered (Phases A–D) as well as their operations cost (Phase E). The estimates were primarily developed using NASA funded cost modeling applications. The Project Cost Estimating Capability (PCEC) model was used to estimate the majority of elements of the Work Breakdown Structure (WBS), while the NASA Instrument Cost Model (NICM) was used to estimate the payload (telescope assembly) portion of the systems. These models take into account recent cost data on space-based spacecraft and instruments, respectively. All costs were estimated in FY17 dollars and can be considered to be near the 50% confidence level. A 5-year development schedule (Phase A-D) was assumed for each of the mission options with the exception of the IR hosted case which was assumed to have a 3-year development schedule. ***Table 3*** shows the parametric models used to estimate each of the system WBS elements.

Table 3 *Cost Models Used by Phase and WBS Element*

WBS #	WBS Description	Phase B-D	Phase E
WBS 1.0	Program Management	PCEC v2.2	-
WBS 2.0	Systems Engineering	PCEC v2.2	-
WBS 3.0	Mission Assurance	PCEC v2.2	-
WBS 4.0	Science	PCEC v2.2	-
WBS 5.0	Payload	NICM VIIc*	-
WBS 6.0	Spacecraft Bus	PCEC v2.2	-
WBS 7.0	Mission Ops. & Data Analysis	PCEC v2.2	PCEC v2.2
WBS 8.0	Launch Vehicle	PCEC v2.2	-
WBS 9.0	Ground Data System	PCEC v2.2	-
WBS 10.0	Integration & Test	PCEC v2.2	-
WBS 11.0	Education/Public Outreach	-	-
WBS 12.0	Reserves (% of Cost)	25%	15%

** PRICE Space Missions, a commericial cost model, was used to estimate the cost the 20cm IR instrument.*

Phase A – Preliminary Concept Analysis

Phase A activities include the preliminary analysis of the mission concept. The cost included for Phase A activities in this study was based on recent Phase A costs for analogous flight missions within the NASA portfolio.

Phase B-D, WBS 1.0/2.0/3.0/10.0 – Project Support Functions

Project level support functions include costs associated with the management and engineering oversight at the top level of the project to ensure accomplishment of overall mission objectives. It also includes the integration and testing of the project's systems, payloads, spacecraft, launch services and mission operations. These costs were estimated for Phase B-D using PCEC v2.2 in this study and relied on inputs such as hardware heritage, organizational structure and power/mass requirements.

Phase B-D, WBS 4.0 – Science

This WBS element typically includes the cost of principal investigators, principal scientists, and instrument specialists. Phase B-D science effort was estimated using the PCEC v2.2 science database which provides level of effort estimates based on historical mission data for each of the NASA program lines. In this particular study, the PCEC database for Astrophysics missions was used to estimate the pre-launch science team. As shown in ***Figure 23***, Pre-launch science team costs are approximately 3% of Phase B-D cost less the launch vehicle. This works out to be roughly

10% of the payload cost (WBS 5.0) on average for the AoA cases. In comparison, SDT used 20% of the payload cost (WBS 5.0) to estimate pre-launch science cost.

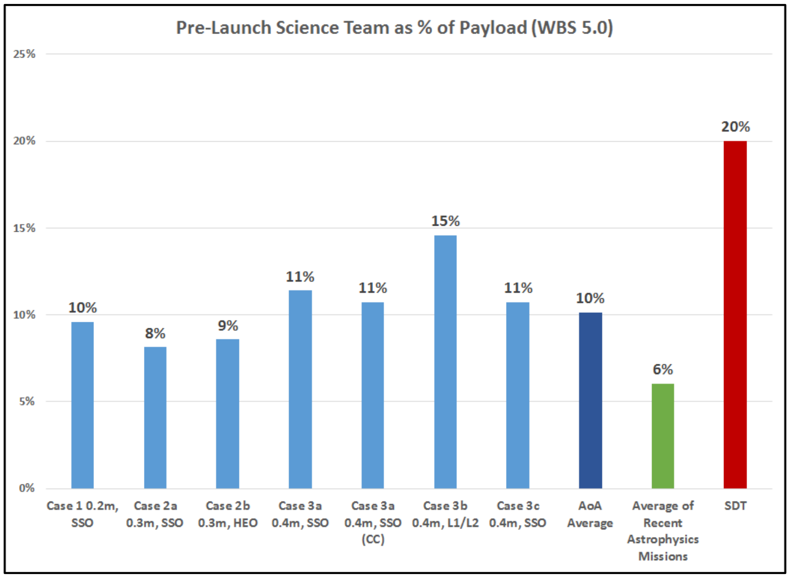

Figure 23 *Pre-launch science team [WBS 4]. The AoA pre-launch science effort is in family with recent NASA Astrophysics missions. Astrophysics mission history ranges from a low of 2% to a high of 14%. Large observatories were excluded from the analogy database.*

Phase B-D, WBS 5.0 – Payload (Telescope Assembly)

Total Phase B-D development costs for each of the instruments were estimated using the current version of the NASA Instrument Cost Model (NICM VIIc) with the exception of the 20-centimeter IR telescope, which was estimated using a commercial model (PRICE™ Space Missions). In the NICM estimated cases, total costs for each instrument were calculated as the sum of two system costs: (1) the optical telescope assembly (OTA) and (2) the back-end instrument (detector, electronics, focal plane array thermal control, and other detector-related subsystems). Standard NICM CERs were used to run Monte Carlo cost simulations (10,000 runs each) for the OTA and detector systems of each instrument option. Aperture diameter was the primary cost driver in the OTA CER, while instrument costs were driven by mass and peak power. All cost estimates assumed a Technology Readiness Level (TRL) for major components and subassemblies of six or greater. No significant technology development efforts were anticipated for any of the instrument options explored.

Phase B-D, WBS 6.0 - Spacecraft Bus

Estimating the costs of spacecraft buses began with defining bus architectures that were capable of providing sustained operation of each instrument option. Most buses were assumed to be Class B, with internally redundant avionics, large propulsion tanks when needed, and additional guidance, navigation, and control elements sufficient for a ten-year design life. All buses were powered by solar arrays, and all relied on monopropellant propulsion systems when needed. Minimal technology development was assumed for the spacecraft bus hardware. These technical parameters along with schedule information were used to drive the estimate using PCEC v2.2. Two of the options considered were costed assuming a significantly shorter life. One of these options was estimated as a Class C mission with a 4-year operational life and the other (20cm hosted IR instrument) was estimated as a Class D mission with a 2-year operational life.

WBS 7.0/9.0 - Mission Operations, Data Analysis and Ground Data System

Phase B-D – Pre-Launch Mission Operations (MOS) & Ground Data System (GDS)

MOS/GDS costs in Phase B-D were estimated using PCEC v2.2. These costs include the system of equipment, software, personnel, procedures, networks, and mission-unique facilities required to conduct mission operations of the spacecraft systems and payloads. ***Figure 24*** shows the comparison of pre-launch MOS/GDS for historical astrophysics missions and the AoA study.

.

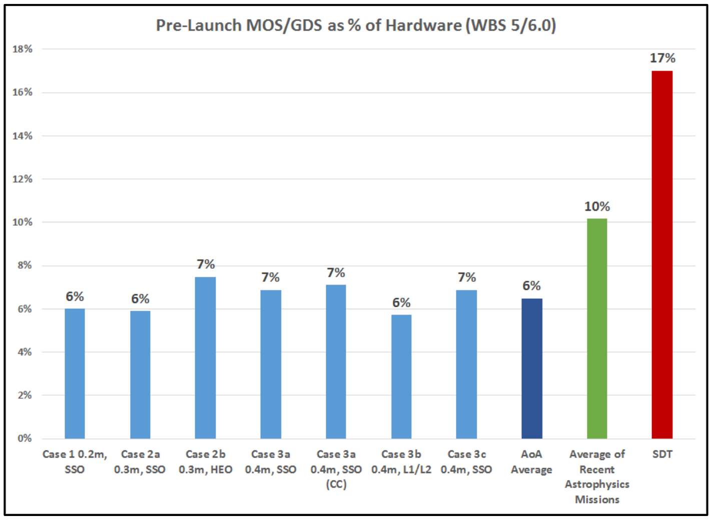

Figure 24 *MOS/ GDS Costs. AoA pre-launch MOS/GDS effort is in family with recent NASA Astrophysics missions. Astrophysics mission history ranges from a low of 5% to a high of 19%. Large observatories were excluded from the analogy database. The numbers are consistent with "operations" type of mission.*

Phase E – Post-Launch Mission Operations & Data Analysis (MO&DA)

MO&DA costs include the management, engineering, and mission operations of the spacecraft and instrument, data communications, and the processing and storage of scientific data. These costs were estimated using PCEC v2.2, assuming a 10-year operational lifetime for most mission options. The Class C case (3a, CC) was assumed to have a 4-year operational lifetime. Many of the model input parameters were minimized in order to capture the operational mission architecture envisioned for each of the options considered. Since PCEC does not estimate the cost of telecommunications services, including telemetry and downloads of science data, those costs were calculated separately on the basis of the network used and were included in the Phase E estimate. It was assumed that most of the mission cases made use of the Near Earth Network (NEN).

Phase B-D, WBS 8.0 – Launch Vehicle (LV)

PCEC along with publicly available pricing information, was used to estimate the cost of the launch vehicles and services for each of the mission options. Continued disruption in the LV market will likely exert downward pressure on the overall cost to orbit.

Phase B-E, WBS 11.0 – Education and Public Outreach (E/PO)

Education and Public Outreach efforts were not considered in this analysis. Historically, E/PO funding has been 1-2% of the total mission cost.

Phase A-E, WBS 12.0 – Reserves

Unallocated cost reserves were added to the baseline cost estimate, a conservative strategy that, together with the absence of technology development, should ensure a successful mission. Reserves were calculated on a percentage basis by phase and were based on historical reserve postures of recent NASA space flight missions. No reserve was included for Phase A, 25% reserve was included for Phases B-D and 15% for Phase E.

Cost Summary

The total costs for the cases of interest are shown in ***Figure 25***. They cover Phases A-D but do not incorporate the Launch Vehicle costs, per AoA direction. They include both "detection and tracking" and "characterization", and thus contain both a 0.2 m IR hosted payload (Case 5) together with a VIS system (signified by Case 'X', e.g. Case 3a). These costs are mostly over the stated $400 M goal, however, like the SDT's costs, they are model-based with generalized assumptions and do not have the benefits of Phase A investments, e.g. NEOCam. Selecting between competing approaches and their costs will require validated models to support performance claims. Additional detail on costs and their comparison with SDT results are shown in **Appendix C**.

Phase A-D Cost w/o LV (FY17$k) of IR Case 5 + Visible Case "X"	Visible Telescopes						
	Case 1	Case 2a	Case 2b	Case 3a	Case 3a	Case 3b	Case 3c
	0.2	0.3	0.3	0.4	0.4	0.4	0.4
	SSO	SSO	HEO	SSO	SSO (CC)	L1	SSO
IR Telescope Case 5 0.2 GEO	$ 422,552	$ 454,664	$ 470,927	$ 407,017	$ 386,184	$ 481,776	$ 301,103

% Difference Between Identified Scearios and $400M (FY17$k)	Visible Telescopes						
	Case 1	Case 2a	Case 2b	Case 3a	Case 3a	Case 3b	Case 3c
	0.2	0.3	0.3	0.4	0.4	0.4	0.4
	SSO	SSO	HEO	SSO	SSO (CC)	L1	SSO
IR Telescope Case 5 0.2 GEO	6%	14%	18%	2%	-3%	20%	-25%

Figure 25 Cost summary for the cases of interest. They show both the total costs and the difference between the identified scenarios and the $400 M (FY17).

7.0 Conclusions

The results from the SDT 2017 study are certainly the most comprehensive to date. The NEO AoA focused on looking for less expensive alternatives, however, it did not reach any conclusive results to provide an alternative approach. Observations and lessons learned are shared below.

Models

The NEO community has one mature IR "anchor" model (JPL), used for SDT, that has benefited from more than a decade of NASA investment, calibration and validation using flight data from NEOWise. Other IR models exist, but have much less fidelity. The NEO AoA results for the same sensor and strategy are more pessimistic, but also have less fidelity than the "anchor" model. For visible, the NEO community has 3 models that approach the problem differently, and results to date have some variability. The models are from Lincoln Labs MIT (used for SDT), JHU/APL, and GSFC. All of these models are in evolving state of maturity. There is no "anchor" model to evaluate visible systems. AoA recommendation is to standardize visible approach and fund MIT/LL or GSFC to provide a fully calibrated/validated "anchor" model that would iron out the discrepancies between the visible models. This anchor model will not guarantee a different result, but the method for performance assessment will be sound.

Solutions

A multitude of survey solutions and methods to approach the problem exist, given state of current technology. All have pros and cons. The AoA did not find much less expensive options than those presented in the SDT report. For visible, smaller telescope options exist, and while they do not appear to meet the requirement, they might still be impacted by the model fidelity (validation problem) stated above. Using a 0.2 m hosted IR telescope in GEO for characterization of already catalogued objects might be feasible, and additional work can be done (e.g. tuning the wavelength bands). With the commercial market, additional hosting opportunities are becoming rapidly available and more are anticipated. Additionally, separating characterization from detection and tracking might allow for more flexibility in launch schedule and phasing, as well as for maturity of the IR sensor technology. AoA recommends to gather a forum on NEO characterization to understand what is adequate to meet policy, and if measurements in IR and Visible wavelength bands can contribute to solution. As far as using small visible telescopes for CubeSats, there is promise, but better attitude and data solutions have to be implemented before it becomes feasible.

References

- M. Granvik, A. Morbidelli, R. Jedicke, B. Bolin, W. F. Bottke, EBeshore, D. Vokrouhlicky, M. Delbo, and P. Michel. *Nature* 530:303 (2016).

- Mainzer, A.K., Bauer, J.M., Cutri, R.M., Grav, T., Kramer, E.A., Masiero, J.R., Nugent, C.R., Sonnett, S.M., Stevenson, R.A., and Wright, E.L., NEOWISE Diameters and Albedos V1.0. EAR-A-COMPIL-5-NEOWISEDIAM-V1.0. NASA Planetary Data System, 2016.
- B.D. Warner, A.W. Harris, and P. Pravec. Icarus 202:134-146, (2009). Updated 2017 April 3. http://www.MinorPlanet.info/lightcurvedatabase.html
- W. Harris, *Icarus* 131:291 (1998).
- L. A. Lebofsky and J. R. Spencer. "Radiometry and thermal modeling of asteroids." In *Asteroids II* (R. P. Binzel, T. Gehrels, and M. S. Matthews, Eds.), pp. 128–147. Univ. of Arizona Press, Tucson, 1989.
- "Background Model," http://irsa.ipac.caltech.edu/applications/BackgroundModel. Version 4, Aug. 2017.
- E. L. Wright, *Astrophys. J.* 496:1 (1998).
- V. Gorjian, E. L. Wright, and R. R. Chary, *Astrophys. J.* 536:550 (2000).
- K. Krisciunas and B. E. Schaefer. *Publ. Astron. Soc. Pacific* 103:1033 (1991).
- "Seeing," https://www.naoj.org/Observing/Telescope/ImageQuality/Seeing. Accessed June 2017.
- R. Wainscoat, Optimizing Search Strategies for Near Earth Objects: Lessons Learned from Pan-STARRS1, IEEE Aerospace Conference, 03/2017. DOI: 10.1109/AERO.2017.7943958.
- Shao, M., S. Turyshev, S. Spangelo,T. Werne, C. Zhai., A constellation of CubeSats with synthetic tracking cameras to search for 90% of potentially hazardous near-Earth objects, Astronomy &Astrophysics, 603, A126, 2017.
- R. Wainscoat, The Pan-STARRS search for Near Earth Objects, IEEE Aerospace Conference, Big Sky, MT, March 2016. DOI: 10.1109/AERO.2016.7500568.
- D. J. Dichmann, J. J. K. Parker, T. W. Williams, C. R. Mendelsohn, "Trajectory Design for the Transiting Exoplanet Survey Satellite," 24th International Symposium on Space Flight Dynamics, Laurel, MD, 2014.
- Tennant, W.E. et al., MBE HgCdTe Technology: A Very General Solution to IR Detection, Described by "Rule 07", a Very Convenient Heuristic, 37, p.1406-1410, J. Electronic Materials, 2008.
- "ORS-5 SensorSat Performance Analysis." MIT LL. 2015-09-10. Version 1.1
- C. J. Willers and M. S. Willers, Proc. SPIE 10036, 4th Conference for Sensors, MEMS, and Electro-Optic Systems, 100360S (2017): gives typical γ_M values of 1-5% for vis, 5-15% for SWIR and 20-30% for MWIR
- S. Hanna et al, J. Electron. Mater. 45:4543 (2016): 1.2% γ_M reported as an "advancement in detector technology" for a HgCdTe LWIR sensor
- M. Schulz and L. Caldwell, Infrared Phys. Technol 36:763 (1995): typical γ_M is >10% for compound semiconductors; can get to 10^-4 with correction, but maintaining this level requires recalibration every few minutes to hours (depending on the device) [note this paper is quite old for the field]

Appendix A

AOA Team Members

Core Team Member/ Report Author	Role/ Affiliation
Elena Adams	Systems Engineer/ Spacecraft, JHU/APL
Nishant Mehta	Model Lead, JHU/APL
Carolyn Sawyer	Model, JHU/APL
Amanda Haapala Chalk	Trajectory design, observational strategy, JHU/APL
Ed Hawkins	Payload, JHU/APL
Mike Cully	Manager, JHU/APL
Shawn Hayes	Cost Estimator, Space System Analysists

Other Contributors	Role/ Affiliation
Simon Wing	Data analysis, JHU/APL
Joseph Linden	Optical Design, JHU/APL
Hugo Darlington	Optical Detectors, JHU/APL
Matt Grey	Payload DPU, JHU/APL
Jed Hancock	Optical/System, SDL
Erik Syrstad	Payload Cost Modeling, SDL
Roy Esplin	Optical Design, SDL
Scott Hansen	Radiometric Analysis, SDL
Brian Thompson	Mechanical/ Systems, SDL
Arnie Goldberg	IR detectors, JHU/APL
Joe Centurelli	Fast steering mirror design, JHU/APL
Dawn Moessner	Mission Design, JHU/APL
Brian Lathrop	Mission Design, JHU/APL
Rob Clark	Contact, Harris Corporation
Andy Rivkin	Science consultant, JHU/APL
Andy Cheng	Science consultant, JHU/APL
Deva Ponnusamy	Mechanicla s/c design, JHU/APL
Stewart Bushman	Propulsion s/c design, JHU/APL
Geff Ottman	Avionics s/c design, JHU/APL
Gabe Rogers	GNC s/c design, JHU/APL
Brian Sequeira	Comms s/c design, JHU/APL
Mike Marley/ Alan Holtzman	Thermal s/c design, JHU/APL
Faith Kujawa	Hosted Payload Research, JHU/APL
Michelle Chen	Software Algorithms Lead, JHU/APL
Musad Haque	Software Algorithms, JHU/APL
Jared Markowitz	Software Algorithms, JHU/APL
Rob Pattay	Software Algorithms, JHU/APL
Todd Hurt	Software Algorithms, JHU/APL
Syau-Yun Hsieh	Software Algorithms, JHU/APL
Timothy Miller	Software Algorithms, JHU/APL
Meagan Hahn	Cost Estimator, JHU/APL
Rachel Sholder	Cost Estimator, JHU/APL
Cheryl Reed	Project Manager, JHU/APL

Appendix B: Margin Summary for Studied Cases

Case 1: 0.2m Quad Visible Telescopes for Detection and Tracking in Sun Sync Orbit

20cm Quad VIS @ SSO Flight System Mass Summary			
Subsystem	**CBE**	**Cont.**	**MEV**
Structures	49 kg	9%	53 kg
Propulsion	14 kg	4%	15 kg
Avionics	18 kg	4%	18 kg
Electrical Power	39 kg	8%	42 kg
Attitude Determination and Control	23 kg	3%	24 kg
Thermal Control	13 kg	10%	14 kg
RF Communications	19 kg	3%	20 kg
Harness	12 kg	7%	13 kg
Spacecraft Bus Total	**187 kg**	**7%**	**199 kg**
Payload	**40 kg**	**25%**	**50 kg**
Total Dry Mass	**227 kg**	**10%**	**249 kg**
Contingency			**23 kg**
% Contingency			**10%**
Maximum Possible Dry Mass			**764 kg**
Dry Mass Margin			**515 kg**
% Dry Mass Margin			**207%**
Total Dry Mass Margin (Unallocated and Contingency)			**237%**
Propellant and Residuals			16 kg
Total MPV Wet Mass			**780 kg**
Launch Vehicle Capability, SSO, Taurus 3210 (92 in fairing)			780 kg

Maneuver	**Deterministic ΔV (m/s)**	**Statistical ΔV (m/s)**	**Total ΔV (m/s)**
Launch		20	20
Station Keeping	31.5	1	32
Disposal/ De-orbit	50	2	52
		Total	**104**

Case 2a: 0.3m Quad Visible Telescopes for Detection and Tracking in Sun Sync Orbit

30cm Quad VIS @ SSO Flight System Mass Summary			
Subsystem	**CBE**	**Cont.**	**MEV**
Structures	69 kg	9%	75 kg
Propulsion	14 kg	4%	15 kg
Avionics	18 kg	4%	18 kg
Electrical Power	57 kg	9%	62 kg
Attitude Determination and Control	28 kg	3%	29 kg
Thermal Control	15 kg	10%	16 kg
RF Communications	19 kg	3%	20 kg
Harness	15 kg	7%	16 kg
Spacecraft Bus Total	**235 kg**	**7%**	**251 kg**
Payload	**102 kg**	**25%**	**127 kg**
Total Dry Mass	**336 kg**	**12%**	**378 kg**
Contingency			**42 kg**
% Contingency			**12%**
Maximum Possible Dry Mass			**759 kg**
Dry Mass Margin			**381 kg**
% Dry Mass Margin			**101%**
Total Dry Mass Margin (Unallocated and Contingency)			**126%**
Propellant and Residuals			21 kg
Total MPV Wet Mass			**780 kg**
Launch Vehicle Capability, SSO, Taurus 3210 (92 in fairing)			780 kg

Maneuver	Deterministic ΔV (m/s)	Statistical ΔV (m/s)	Total ΔV (m/s)
Launch		20	20
Station Keeping	31.5	1	32
Disposal/ De-orbit	50	2	52
Total			**104**

Case 2b: 0.3m Quad Visible Telescopes for Detection and Tracking in High Altitude Earth (HEO) Orbit

30cm Quad VIS @ HEO (TESS) Flight System Mass Summary			
Subsystem	**CBE**	**Cont.**	**MEV**
Structures	78 kg	10%	85 kg
Propulsion	18 kg	4%	18 kg
Avionics	12 kg	4%	12 kg
Electrical Power	64 kg	9%	70 kg
Attitude Determination and Control	28 kg	3%	29 kg
Thermal Control	20 kg	10%	22 kg
RF Communications	29 kg	5%	30 kg
Harness	17 kg	8%	18 kg
Spacecraft Bus Total	**265 kg**	**8%**	**285 kg**
Payload	**102 kg**	**25%**	**127 kg**
Total Dry Mass	**366 kg**	**12%**	**412 kg**
Contingency			**46 kg**
% Contingency			**12%**
Maximum Possible Dry Mass			**1539 kg**
Dry Mass Margin			**1127 kg**
% Dry Mass Margin			**274%**
Total Dry Mass Margin (Unallocated and Contingency)			**320%**
Propellant and Residuals			51 kg
Total MPV Wet Mass			**1590 kg**
Launch Vehicle Capability (C3 of -2.8 km2/s2), Antares 232			1590 kg

Maneuver	Deterministic ∆V (m/s)	Statistical ∆V (m/s)	Total ∆V (m/s)
Launch		20	20
Peri-raise maneuver	30	1	30
Apoapse raise maneuver	38	21	59
Apoapse raise maneuver	20	1	21
Translunar injection maneuver	4	22	26
Period Adjust maneuver	86	3	88
EOL maneuver		10	10
ACS			*3*
Total			**237**

Case 3a: 0.4m Visible Telescopes for Detection and Tracking in L1 orbit

40cm VIS @ SSO Flight System Mass Summary			
Subsystem	**CBE**	**Cont.**	**MEV**
Structures	53 kg	9%	58 kg
Propulsion	14 kg	4%	15 kg
Avionics	18 kg	4%	18 kg
Electrical Power	45 kg	9%	49 kg
Attitude Determination and Control	28 kg	3%	29 kg
Thermal Control	13 kg	10%	14 kg
RF Communications	19 kg	3%	20 kg
Harness	13 kg	7%	14 kg
Spacecraft Bus Total	**202 kg**	**7%**	**216 kg**
Payload	**51 kg**	**25%**	**64 kg**
Total Dry Mass	**253 kg**	**10%**	**280 kg**
Contingency			**27 kg**
% Contingency			**10%**
Maximum Possible Dry Mass			**764 kg**
Dry Mass Margin			**484 kg**
% Dry Mass Margin			**173%**
Total Dry Mass Margin (Unallocated and Contingency)			**201%**
Propellant and Residuals			16 kg
Total MPV Wet Mass			**780 kg**
Launch Vehicle Capability, SSO, Taurus 3210 (92 in fairing)			780 kg

Maneuver	Deterministic ΔV (m/s)	Statistical ΔV (m/s)	Total ΔV (m/s)
Launch		20	20
Station Keeping	31.5	1	32
Disposal/ De-orbit	50	2	52
		Total	**104**

Case 3b: 0.4m Visible Telescopes for Detection and Tracking in L1 orbit

40cm VIS @ L1 Flight System Mass Summary			
Subsystem	**CBE**	**Cont.**	**MEV**
Structures	57 kg	10%	63 kg
Propulsion	14 kg	4%	15 kg
Avionics	18 kg	4%	18 kg
Electrical Power	49 kg	9%	53 kg
Attitude Determination and Control	28 kg	3%	29 kg
Thermal Control	15 kg	10%	16 kg
RF Communications	29 kg	5%	30 kg
Harness	14 kg	7%	15 kg
Spacecraft Bus Total	**224 kg**	**7%**	**239 kg**
Payload	**50 kg**	**25%**	**63 kg**
Total Dry Mass	**274 kg**	**10%**	**302 kg**
Contingency			**28 kg**
% Contingency			**10%**
Maximum Possible Dry Mass			**1486 kg**
Dry Mass Margin			**1184 kg**
% Dry Mass Margin			**392%**
Total Dry Mass Margin (Unallocated and Contingency)			**442%**
Propellant and Residuals			19 kg
Total MPV Wet Mass			**1505 kg**
Launch Vehicle Capability (C3 of -0.61 km2/s2), Antares 232			1505 kg

Maneuver	Deterministic ΔV (m/s)	Statistical ΔV (m/s)	Total ΔV (m/s)
Launch Insertion		20	20
Orbit Insertion	57	1.7	59
Station Keeping	26.3	0.8	27
ACS			3
Total			**106**

Case 5: Follow-on Characterization Payload, 20cm IR

20cm IR follow on, hosted @ GEO Flight System Mass Summary			
Subsystem	**CBE**	**Cont.**	**MEV**
Optical Payload	44 kg	15%	50 kg
Payload Support Structure	11 kg	15%	12 kg
Thermal Control	28 kg	15%	32 kg
Cryocoolers	21 kg	15%	24 kg
Gimbal Assembly	65 kg	15%	75 kg
Reaction Wheel Assembly	20 kg	15%	23 kg
Digital Processing Unit (DPU)	3 kg	15%	3 kg
Harness	8 kg	15%	9 kg
Total Dry Mass	**199 kg**	**15%**	**228 kg**
		Contingency	**30 kg**
		% Contingency	**15%**
		Maximum Possible Dry Mass	**285 kg**
		Dry Mass Margin	**57 kg**
		% Dry Mass Margin	**25%**
		Total Dry Mass Margin (Unallocated and Contingency)	**44%**
Hosted Payload Capability (e.g. Iridium MPV)			285 kg

Appendix C: Cost Details and Comparison to SDT

		AoA								SDT					
		Visible Telescopes							IR Telescope	Visible Telescopes				IR Telescopes	
		Case 1	Case 2a	Case 2b	Case 3a	Case 3a	Case 3b	Case 3c	Case 5	3V	4V	5V	6V	3IR	4IR
	Aperture (m)	0.2	0.3	0.3	0.4	0.4	0.4	0.4	0.2	1.0	1.0	1.0	1.0	0.5	0.5
	Orbit	SSO	SSO	HEO	SSO	SSO (CC)	L1/L2	SSO	GEO	SSO	L1/L2	L1/L2	0.7AU	L1/L2	0.7AU
WBS	Description	50% C.L. Point Estimate (FY17 $M)	50% C.L. Point Estimate (FY17 $M)	50% C.L. Point Estimate (FY17 $M)	50% C.L. Point Estimate (FY17 $M)	50% C.L. Point Estimate (FY17 $M)	50% C.L. Point Estimate (FY17 $M)	50% C.L. Point Estimate (FY17 $M)	50% C.L. Point Estimate (FY17 $M)	50% C.L. Point Estimate (FY17 $M)	50% C.L. Point Estimate (FY17 $M)	50% C.L. Point Estimate (FY17 $M)	50% C.L. Point Estimate (FY17 $M)	50% C.L. Point Estimate (FY17 $M)	50% C.L. Point Estimate (FY17 $M)
Phase A	Phase A Study	$ 3	$ 3	$ 3	$ 3	$ 3	$ 3	$ 3	$ 2	$ 2	$ 2	$ 2	$ 2	$ 1	$ 1
WBS 1.0/2.0/3.0	Project Level - PM/SE/MA	$ 28	$ 28	$ 28	$ 27	$ 23	$ 30	$ 57	$ 32	$ 58	$ 60	$ 78	$ 101	$ 50	$ 79
WBS 4.0	Pre-Launch Science	$ 5	$ 6	$ 6	$ 4	$ 4	$ 6	$ 4	$ 5	$ 23	$ 23	$ 26	$ 31	$ 21	$ 30
WBS 5.0	Payload Roll Up	$ 50	$ 70	$ 70	$ 39	$ 37	$ 40	$ 41	$ 77	$ 115	$ 114	$ 132	$ 155	$ 103	$ 150
WBS 6.0	Spacecraft Roll Up	$ 87	$ 91	$ 100	$ 87	$ 77	$ 140	$ -	$ 81	$ 146	$ 155	$ 218	$ 298	$ 122	$ 202
WBS 7.0/9.0	Mission Ops./Ground Data System	$ 8	$ 9	$ 13	$ 9	$ 8	$ 10	$ 9	$ -	$ 34	$ 35	$ 48	$ 63	$ 29	$ 46
WBS 10.0	System Level IAT	$ 3	$ 4	$ 4	$ 3	$ 3	$ 4	$ 3	$ -	$ 31	$ 32	$ 42	$ 54	$ 27	$ 42
SubTotal Phase A-D		$ 185	$ 211	$ 224	$ 173	$ 156	$ 233	$ 118	$ 196	$ 409	$ 422	$ 545	$ 704	$ 353	$ 551
Reserves Phase A-D		$ 46	$ 53	$ 56	$ 43	$ 39	$ 58	$ 22	$ 22	$ 122	$ 126	$ 163	$ 211	$ 106	$ 165
Total with Reserves Phase A-D w/o LV		$ 232	$ 264	$ 280	$ 216	$ 195	$ 291	$ 140	$ 218	$ 532	$ 548	$ 708	$ 914	$ 459	$ 716
WBS 8.0	Launch Vehicle & Services	$ 57	$ 57	$ 83	$ 57	$ 57	$ 83	$ 57	$ -	$ 147	$ 147	$ 147	$ 184	$ 147	$ 184
Total with Reserves Phase A-D w/ LV		$ 289	$ 321	$ 363	$ 273	$ 252	$ 374	$ 197	$ 218	$ 679	$ 695	$ 855	$ 1,098	$ 606	$ 900
Phase E (WBS 7.0)	MO&DA	$ 66	$ 66	$ 98	$ 68	$ 34	$ 84	$ 68	$ 10	$ 223	$ 223	$ 245	$ 947	$ 139	$ 613
Reserves Phase E		$ 10	$ 10	$ 15	$ 10	$ 5	$ 13	$ 10	$ 1	$ 33	$ 33	$ 37	$ 142	$ 21	$ 92
SubTotal Phase E		$ 76	$ 76	$ 112	$ 79	$ 39	$ 97	$ 79	$ 11	$ 257	$ 257	$ 282	$ 1,089	$ 160	$ 705
Total with Reserves Phase A-E w/ LV		$ 365	$ 397	$ 475	$ 352	$ 292	$ 471	$ 276	$ 229	$ 935	$ 951	$ 1,137	$ 2,187	$ 766	$ 1,605